# The Effect of Combined Magnetic Geometries on Thermally Driven Winds. II. Dipolar, Quadrupolar, and Octupolar Topologies

Adam J. Finley and Sean P. Matt
University of Exeter, Department of Physics & Astronomy, Stoker Road, Devon, Exeter, EX4 4QL, UK; af472@exeter.ac.uk
*Received 2017 November 21; revised 2018 January 18; accepted 2018 January 23; published 2018 February 15*

## Abstract

During the lifetime of Sun-like or low-mass stars a significant amount of angular momentum is removed through magnetized stellar winds. This process is often assumed to be governed by the dipolar component of the magnetic field. However, observed magnetic fields can host strong quadrupolar and/or octupolar components, which may influence the resulting spin-down torque on the star. In Paper I, we used the MHD code PLUTO to compute steady-state solutions for stellar winds containing a mixture of dipole and quadrupole geometries. We showed the combined winds to be more complex than a simple sum of winds with these individual components. This work follows the same method as Paper I, including the octupole geometry, which not only increases the field complexity but also, more fundamentally, looks for the first time at combining the same symmetry family of fields, with the field polarity of the dipole and octupole geometries reversing over the equator (unlike the symmetric quadrupole). We show, as in Paper I, that the lowest-order component typically dominates the spin-down torque. Specifically, the dipole component is the most significant in governing the spin-down torque for mixed geometries and under most conditions for real stars. We present a general torque formulation that includes the effects of complex, mixed fields, which predicts the torque for all the simulations to within 20% precision, and the majority to within $\approx$5%. This can be used as an input for rotational evolution calculations in cases where the individual magnetic components are known.

*Key words:* magnetohydrodynamics (MHD) – stars: low-mass – stars: magnetic field – stars: rotation – stars: winds, outflows

*Supporting material:* machine-readable table

## 1. Introduction

Cool stars are observed to host global magnetic fields that are embedded within their outer convection zones (Reiners 2012). Stellar magnetism is driven by an internal dynamo that is controlled by the convection and stellar rotation rate, the exact physics of which is still not fully understood (see review by Brun & Browning 2017). As observed for the Sun, plasma escapes the stellar surface, interacting with this magnetic field and forming a magnetized stellar wind that permeates the environment surrounding the star (Cranmer et al. 2017). Young main-sequence stars show a large spread in rotation rates for a given mass. As a given star ages on the main sequence, their stellar wind removes angular momentum, slowing the rotation of the star (Schatzman 1962; Weber & Davis 1967; Mestel 1968). This in turn reduces the strength of the magnetic dynamo process, feeding back into the strength of the applied stellar wind torque. This relationship leads to a convergence of the spin rates toward a tight mass–rotation relationship at late ages, as stars with faster rotation incur larger spin-down torques and vice versa for slow rotators. This is observed to produce a simple relation between rotation period and stellar age ($\Omega_* \propto t^{-0.5}$; Skumanich 1972), which is approximately followed, on average (Soderblom 1983), over long timescales.

With the growing number of observed rotation periods (Irwin & Bouvier 2009; Agüeros et al. 2011; Meibom et al. 2011; McQuillan et al. 2013; Bouvier et al. 2014; Stauffer et al. 2016; Davenport 2017), an increased effort has been channeled into correctly modeling the spin-down process (e.g., Reiners & Mohanty 2012; Gallet & Bouvier 2013; Van Saders & Pinsonneault 2013; Brown 2014; Gallet & Bouvier 2015; Matt et al. 2015; Amard et al. 2016; Blackman &

Owen 2016; See et al. 2017a), as it is able to test our understanding of basic stellar physics and also date observed stellar populations.

The process of generating stellar ages from rotation is referred to as gyrochronology, whereby a cluster's age can be estimated from the distribution of observed rotation periods (Barnes 2003; Meibom et al. 2009; Barnes 2010; Delorme et al. 2011; Van Saders & Pinsonneault 2013). This requires an accurate prescription of the spin-down torques experienced by stars as a result of their stellar wind, along with their internal structure and properties of the stellar dynamo. Based on results from magnetohydrodynamic (MHD) simulations, parameterized relations for the stellar wind torque are formulated using the stellar magnetic field strength, mass-loss rate, and basic stellar parameters (Mestel 1984; Kawaler 1988; Matt & Pudritz 2008; Ud-Doula et al. 2009; Pinto et al. 2011; Matt et al. 2012; Réville et al. 2015). The present work focuses on improving the modeled torque on these stars due to their magnetized stellar winds, by including the effects of combined magnetic geometries.

Magnetic field detections from stars, other than the Sun, were reported over 30 yr ago via Zeeman broadening observations (Robinson et al. 1980; Gray 1984; Marcy 1984), a technique that has since been used on a multitude of stars (e.g., Saar 1990; Johns-Krull & Valenti 2000). This technique, however, only allows for an average line-of-sight estimate of the unsigned magnetic flux and provides no information about the geometry of the stellar magnetic field (see review by Reiners 2012). More recently, the use of Zeeman Doppler Imaging (ZDI), a tomographic technique capable of providing information about the photospheric magnetic field of a given

star, enables the observed field to be broken down into individual spherical harmonic contributions (e.g., Hussain et al. 2002; Donati et al. 2006, 2008; Morin et al. 2008a, 2008b; Petit et al. 2008; Fares et al. 2009; Morgenthaler et al. 2011; Jeffers et al. 2014; Vidotto et al. 2014; See et al. 2015, 2016, 2017b; Folsom et al. 2016; Hébrard et al. 2016; Saikia et al. 2016; Kochukhov et al. 2017). This allows the 3D magnetic geometry to be recovered, typically using a combination of field extrapolation and MHD modeling (e.g., Cohen et al. 2011; Vidotto et al. 2011; Alvarado-Gómez et al. 2016; do Nascimento et al. 2016; Garraffo et al. 2016b; Nicholson et al. 2016; Réville et al. 2016).

Pre-main-sequence stars, observed with ZDI, show a variety of multipolar components, typically dependent on the internal structure of the host star (Gregory et al. 2012; Hussain & Alecian 2013). Many of these objects show an overall dipolar geometry with an accompanying octupole component (e.g., Donati et al. 2007; Gregory et al. 2012). The addition of dipole and octupole fields has been explored analytically, for these stars, and is shown to impact the disk truncation radius along with the topology and field strength of accretion funnels (Gregory & Donati 2011; Gregory et al. 2016). For main-sequence stellar winds, the behavior of combined magnetic geometries has yet to be systematically explored. Our closest star, the Sun, hosts a significant quadrupolar contribution during the solar activity cycle maximum that dominates the large-scale magnetic field geometry along with a small dipole component (DeRosa et al. 2012; Brun et al. 2013). The impact of these mixed geometry fields on the spin-down torque generated from magnetized stellar winds remains uncertain.

It is known that the magnetic field stored in the lowest-order geometries, e.g., dipole, quadrupole, and octupole, has the slowest radial decay and therefore governs the strength of the magnetic field at the Alfvén surface (and thus its size and shape). With the cylindrical extent of the Alfvén surface being directly related to the efficiency of the magnetic braking mechanism, it is this global field strength and geometry that are required to compute accurate braking torques in MHD simulations (Réville et al. 2015, 2016). However, the effect of the higher-order components on the acceleration of the wind close in to the star may not be non-negligible (Cranmer & Van Ballegooijen 2005; Cohen et al. 2009). Additionally, the small-scale surface features described by these higher-order geometries (e.g., starspots and active regions) will play a vital role in modulating the chromospheric activity (e.g., Testa et al. 2004; Aschwanden 2006; Güdel 2007; Garraffo et al. 2013), which is often assumed to be decoupled from the open-field regions producing the stellar wind. Models such as the AWESOM (van der Holst et al. 2014) include this energy dissipation in the lower corona and are able to match observed solar parameters well. Work by Pantolmos & Matt (2017) shows how this additional acceleration can be accounted for globally within their semianalytic formulations.

Previous works have aimed to understand the impact of more complex magnetic geometries on the rotational evolution of Sun-like stars. Holzwarth (2005) examined the effect of nonuniform flux distributions on the magnetic braking torque, investigating the latitudinal dependence of the stellar wind produced within their MHD simulations. Similarly, Garraffo et al. (2016a) included magnetic spots at differing latitudes and examined the resulting changes to mass-loss rate and spin-down torque. The effectiveness of the magnetic braking

from a stellar wind is found to be reduced for higher-order magnetic geometries (Garraffo et al. 2015). This is explained in Réville et al. (2015) as a reduction to the average Alfvén radius, which acts mathematically as a lever arm for the applied braking torque. Finley & Matt (2017, hereafter Paper I) continue this work by discussing the morphology and braking torque generated from combined dipolar and quadrupolar field geometries using ideal MHD simulations of thermally driven stellar winds. In this current work, we continue this mixed-field investigation by including combinations with an octupole component.

Section 2 introduces the simulations and the numerical methods used, along with our parameterization of the magnetic field geometries and derived simulation properties. Section 3 explores the resulting relationship of the average Alfvén radius with increasing magnetic field strength for pure fields, as well as generic combinations of axisymmetric dipole, quadrupole, or octupole geometries. Section 4 uses the decay of the unsigned magnetic flux with distance to explain observed behaviors in our Alfvén radii relations; analysis of the open magnetic flux in our wind solutions follows with a singular relation for predicting the average Alfvén radius based on the open flux. Conclusions and thoughts for future work can be found in Section 5.

## 2. Simulation Method and Numerical Setup

As in Paper I, we use the PLUTO MHD code (Mignone et al. 2007; Mignone 2009) with a spherical geometry to compute 2.5D (two dimensions, $r$, $\theta$, and three vector components, $r$, $\theta$, and $\phi$) steady-state wind solutions for a range of magnetic geometries.

The full set of ideal MHD equations are solved, including the energy equation and a closing equation of state. The internal energy density $\epsilon$ is given by $\rho\epsilon = p/(\gamma - 1)$, where $\gamma$ is the ratio of specific heats. This general set of equations is capable of capturing nonadiabatic processes, such as shocks; however, the solutions found for our steady-state winds generally do not contain these. For a gas composed of protons and electrons $\gamma$ should take a value of $5/3$; however, we decrease this value to 1.05 in order to reproduce the observed near-isothermal nature of the solar corona (Steinolfson & Hundhausen 1988) and a terminal speed consistent with the solar wind. This is done, such that on large scales the wind follows the polytropic approximation, i.e., the wind pressure and density are related as $p \propto \rho^\gamma$ (Parker 1965; Keppens & Goedbloed 1999). The reduced value of $\gamma$ has the effect of artificially heating the wind as it expands, without an explicit heating term in our equations.

We adopt the numerics used in Paper I, except that we modify the radial discretization of the computational mesh. Instead of a geometrically stretched radial grid as before, we now employ a stepping ($dr$) that grows logarithmically. The domain extent remains unchanged, from one stellar radius ($R_*$) to $60\,R_*$, containing $N_r \times N_\theta = 256 \times 512$ grid cells. This modification produces a more consistent aspect ratio between $dr$ and $rd\theta$ over the whole domain, which marginally increases our numerical accuracy and stability.

Characteristic speeds such as the surface escape speed and Keplerian speed, $v_{esc}$ and $v_{kep}$, and the equatorial rotation speed, $v_{rot}$, along with the surface adiabatic sound speed, $c_s$,

**Table 1**
Fixed Simulation Parameters

| Parameter | Value | Description |
|---|---|---|
| $\gamma$ | 1.05 | Polytropic index |
| $c_s/v_{esc}$ | 0.25 | Surface sound speed/escape speed |
| $f$ | 4.46E-03 | Fraction of breakup rotation |

and Alfvén speed, $v_A$, are given as follows:

$$v_{esc} = \sqrt{\frac{2GM_*}{R_*}} = \sqrt{2}\, v_{kep}, \qquad (1)$$

where $G$ is the gravitational constant, $R_*$ is the stellar radius, and $M_*$ is the stellar mass;

$$v_{rot} = \Omega_* R_*, \qquad (2)$$

where $\Omega_*$ is the angular stellar rotation rate (which is assumed to be in solid-body rotation);

$$c_s = \sqrt{\frac{\gamma p_*}{\rho_*}}, \qquad (3)$$

where $\gamma$ is the polytropic index and $p_*$ and $\rho_*$ are the gas pressure and mass density at the stellar surface, respectively; and

$$v_A = \frac{B_*}{\sqrt{4\pi\rho_*}}, \qquad (4)$$

where $B_*$ is the characteristic polar magnetic field strength (see Section 2.1).

We set an initial wind speed within the domain using a spherically symmetric Parker wind solution (Parker 1965), with the ratio of the surface sound speed to the escape speed $c_s/v_{esc}$ setting the base wind temperature in such a way as to represent a group of solutions for differing gravitational field strengths. The same normalization is applied to the surface magnetic field strength with $v_A/v_{esc}$, and the surface rotation rate using $f = v_{rot}/v_{kep}$, such that each wind solution represents a family of solutions that can be applied to a range of stellar masses. The same system of input parameters is used by many previous authors (e.g., Matt & Pudritz 2008; Matt et al. 2012; Réville et al. 2015; Pantolmos & Matt 2017). For this study we fix the wind temperature and stellar rotation at the values tabulated in Table 1.

A background field corresponding to our chosen potential magnetic field configuration (see Section 2.1) is imposed over the initial wind solution, and then all quantities are evolved to a steady-state solution by the PLUTO code. The boundary conditions are enforced, as in Paper I, at the inner radial boundary (stellar surface), which are appropriate to give a self-consistent wind solution for a rotating magnetized star. A fixed surface magnetic geometry is therefore maintained along with solid-body rotation.

The use of a polytropic wind produces solutions that are far more isotropic than observed for the Sun (Vidotto et al. 2009). The velocity structure of the solar wind is known to be largely bimodal, having a slow and fast component that originate under different circumstances (Fisk et al. 1998; Feldman et al. 2005; Riley et al. 2006). This work and previous studies using a polytropic assumption aim to model the globally averaged wind, which can be more generally applied to the variety of observed stellar masses and rotation periods. More complex wind driving and heating physics are needed in order to reproduce the observed velocity structure of the solar wind; however, they are far harder to generalize for other stars (Cranmer et al. 2007; Pinto et al. 2016).

## 2.1. Magnetic Field Configurations

The magnetic geometries considered in this work include dipole, quadrupole, and octupole combinations, with different field strengths and in some cases relative orientations. As in Paper I, we describe the mixing of different field geometries using the ratio of the polar field strength in a given component to the total field strength. Care is taken to parameterize the field combinations due to the behavior of the two equatorially antisymmetric components, dipole and octupole, at the poles.

We generalize the ratio defined within Paper I for each component such that

$$\mathcal{R}_x = \frac{B_*^{l=x}}{|B_*^{l=1}| + |B_*^{l=2}| + |B_*^{l=3}|} = \frac{B_*^{l=x}}{B_*}, \qquad (5)$$

where in this work $l$ is the principle spherical harmonic number and $x$ can be 1, 2, or 3 for dipole, quadrupole, or octupole fields. The polar field strength of a given component is written as $B_*^{l=x}$, and the $B_* = |B_*^{l=1}| + |B_*^{l=2}| + |B_*^{l=3}|$ is a characteristic field strength. The polar field strengths in the denominator are given with absolute values because we are interested in the characteristic strength of the combined components, which are the same for aligned and anti-aligned fields. Therefore, summing the absolute value of the ratios produces unity,

$$\sum_{l=1}^{3} |\mathcal{R}_l| = 1, \qquad (6)$$

which allows the individual values of $\mathcal{R}_{dip}$, $\mathcal{R}_{quad}$, and $\mathcal{R}_{oct}$ ($\equiv \mathcal{R}_1$, $\mathcal{R}_2$ and $\mathcal{R}_3$) to range from 1 to $-1$ (north pole positive or negative), with the absolute total remaining constant. We define the magnetic field components using these ratios and the Legendre polynomials $P_{lm}$, which for the axisymmetric ($m = 0$) field components can be written as

$$B_r(r, \theta) = B_* \sum_{l=1}^{3} \mathcal{R}_l P_{l0}(\cos\theta)\left(\frac{R_*}{r}\right)^{l+2}, \qquad (7)$$

$$B_\theta(r, \theta) = B_* \sum_{l=1}^{3} \frac{1}{l+1}\mathcal{R}_l P_{l1}(\cos\theta)\left(\frac{R_*}{r}\right)^{l+2}. \qquad (8)$$

The northern polar magnetic field strengths for each component are given by

$$B_*^{l=1} = \mathcal{R}_{dip}B_*, \quad B_*^{l=2} = \mathcal{R}_{quad}B_*, \quad B_*^{l=3} = \mathcal{R}_{oct}B_*, \qquad (9)$$

The relative orientation of the magnetic components is controlled throughout this work by setting the dipole and quadrupole fields ($B_*^{l=1}$ and $B_*^{l=2}$) to be positive at the northern stellar pole. The octupole component ($B_*^{l=3}$) is then combined with the dipolar and quadruplar components using either a positive or negative strength on the north pole, which we define as the aligned and anti-aligned cases, respectively.

The addition of dipole and quadrupole components was explored in Paper I. We showed the fields to add in one hemisphere and subtract in the other. Similar to the dipole, the octupole component belongs in the "primary" symmetry

family, having antisymmetric field polarity about the equator (McFadden et al. 1991). The addition of any primary geometries with any "secondary" family quadrupole (equatorially symmetric) would be expected to behave qualitatively similarly. A different behavior is expected from the addition of the two primary geometries (dipole–octupole). Here the field addition and subtraction are primarily governed by the relative orientations of the field with respect to one another. Aligned fields will combine constructively over the pole and subtract from one another in the equatorial region. Anti-aligned primary fields, conversely, will subtract on the pole and add over the equator.

Including the results from Paper I, this work includes combinations of all the possible permutations of the axisymmetric dipole, quadrupole, and octupole magnetic geometries. Table 2 contains a complete list of stellar parameters for the cases computed within this work. Parameters for the dipole–quadrupole combined field cases are available in Table 1 of Paper I. It is noted that in the course of the current work the pure dipolar and quadrupole cases are resimulated; see Table 2.

### 2.2. Derived Stellar Wind Properties

The simulations produce steady-state solutions for density, $\rho$, pressure, $p$, velocity, $v$, and magnetic field strength, $B$, for each stellar wind case. From these results, the behavior of the spin-down torque is ascertained. The torque on the star, $\tau$, due to the loss of angular momentum in the stellar wind is calculated as

$$\tau = \int_A \Lambda \rho v \cdot dA, \tag{10}$$

where the angular momentum flux, given by $F_{\rm AM} = \Lambda \rho v$ (Keppens & Goedbloed 2000), is integrated over spherical shells of area $A$ (outside the closed-field regions). $\Lambda$ is given by

$$\Lambda(r, \theta) = r \sin\theta \left( v_\phi - \frac{B_\phi}{\rho} \frac{|B_p|^2}{v_p \cdot B_p} \right). \tag{11}$$

Similarly, the mass-loss rate from our wind solutions is calculated as

$$\dot{M} = \int_A \rho v \cdot dA. \tag{12}$$

An average Alfvén radius is then defined, in terms of the torque, mass-loss rate $\dot{M}$, and rotation rate $\Omega_*$:

$$\langle R_{\rm A} \rangle \equiv \sqrt{\frac{\tau}{\dot{M}\Omega_*}}, \tag{13}$$

In this formulation, $\langle R_{\rm A} \rangle / R_*$ is defined as a dimensionless efficiency factor, by which the magnetized wind carries angular momentum from the star, i.e., a larger average Alfvén radius produces a larger torque for a fixed rotation rate and mass-loss rate,

$$\tau = \dot{M}\Omega_* R_*^2 \left( \frac{\langle R_{\rm A} \rangle}{R_*} \right)^2. \tag{14}$$

In ideal MHD, $\langle R_{\rm A} \rangle$ is associated with a cylindrical Alfvén radius, which acts like a "lever arm" for the spin-down torque on the star.

The methodology of this work follows closely that of Paper I, in which we produce semianalytic formulations for $\langle R_{\rm A} \rangle$ in terms of the wind magnetization, $\Upsilon$, as defined in

previous works (Matt & Pudritz 2008; Matt et al. 2012; Réville et al. 2015; Pantolmos & Matt 2017),

$$\Upsilon = \frac{B_*^2 R_*^2}{\dot{M} v_{\rm esc}}, \tag{15}$$

where $B_*$ is now the characteristic polar field, which is split among the different geometries using the ratios $\mathcal{R}_{\rm dip}$, $\mathcal{R}_{\rm quad}$, and $\mathcal{R}_{\rm oct}$. The values of $\Upsilon$ produced from the steady-state solutions are indirectly controlled by increasing the value of $v_{\rm A}/v_{\rm esc}$. This increases the polar magnetic field strength for a given density normalization. The mass-loss rate is similarly uncontrolled and evolves to steady state, depending mostly on our choice of Parker wind parameters, but is also adjusted self-consistently by the magnetic field. The values of $\Upsilon$ are tabulated in Table 2, along with $\mathcal{R}_l$ values, magnetic field strengths given by $v_{\rm A}/v_{\rm esc}$, and the average Alfvén radii for each case simulated. Results for combined dipole–quadrupole cases are available in Table 1 of Paper I. Figure 1 shows the parameter space of simulations with their value of $\Upsilon$ against the different ratios for either quadrupole–octupole or dipole–octupole cases, with the lower-order geometry ratio labeling the cases ($\mathcal{R}_{\rm quad}$ and $\mathcal{R}_{\rm dip}$, respectively).

## 3. Wind Solutions and $\langle R_{\rm A} \rangle$ Scaling Relations

### 3.1. Single Geometry Winds

For single magnetic geometries, increasing the complexity of the field decreases the effectiveness of the magnetic braking process by reducing the average Alfvén radius (braking lever arm) for a given field strength (Garraffo et al. 2015). The impact of changing field geometries on the scaling of the Alfvén radius for thermally driven winds was shown by Réville et al. (2015) for the dipole, quadrupole, and octupole geometries. We repeat the result of Réville et al. (2015) for a slightly hotter coronal temperature wind, $c_{\rm s} = 0.25$ in our cases, compared to $c_{\rm s} = 0.222$. This temperature more reasonably approximates the solar wind terminal velocity, typically resulting in a wind speed of $\approx 500 \, {\rm km \, s}^{-1}$ at 1 au for solar parameters. For each magnetic geometry, we simulate eight different field strengths, changing the input value of $v_{\rm A}/v_{\rm esc}$ as tabulated in Table 2 (cases 1–24).

Each wind solution gives a value for the Alfvén radius, $\langle R_{\rm A} \rangle$, and the wind magnetization, $\Upsilon$. These values are represented in Figure 2 as colored circles, and their scaling can be described using the Alfvén radius relation from Matt & Pudritz (2008), with three precise power-law relations for the different magnetic geometries, as found previously in the work of Réville et al. (2015):

$$\frac{\langle R_{\rm A} \rangle}{R_*} = K_{\rm s} \Upsilon^{m_{\rm s}}, \tag{16}$$

where $K_{\rm s}$ and $m_{\rm s}$ are fit parameters for this relation, which utilizes the surface field strength. Best-fit parameters for each geometry are tabulated in Table 3.

With increasing $l$ values, the higher-order geometries produce increasingly shallow slopes with wind magnetization, such that they approach a purely hydrodynamical lever arm, i.e., the wind carries away angular momentum corresponding to the surface rotation alone, with the torque efficiency equal to the average cylindrical radius of the stellar surface from the

**Table 2**
Input Parameters and Results from Simulations with One and Two Magnetic Components

| Case | $\mathcal{R}_{dip}\|\mathcal{R}_{quad}\|\mathcal{R}_{oct}$ | $v_A/v_{esc}$ | $\langle R_A \rangle/R_*$ | $\Upsilon$ | $\Upsilon_{open}$ | $\langle v(R_A)\rangle/v_{esc}$ | Case | $\mathcal{R}_{dip}\|\mathcal{R}_{quad}\|\mathcal{R}_{oct}$ | $v_A/v_{esc}$ | $\langle R_A \rangle/R_*$ | $\Upsilon$ | $\Upsilon_{open}$ | $\langle v(R_A)\rangle/v_{esc}$ |
|------|------|------|------|------|------|------|------|------|------|------|------|------|------|
| 1 | 1.0\|0.0\|0.0 | 0.5 | 5.0 | 185 | 1460 | 0.22 | 65 | 0.5\|0.0\|0.5 | 0.5 | 3.8 | 203 | 648 | 0.17 |
| 2 | 1.0\|0.0\|0.0 | 1.0 | 6.9 | 735 | 3540 | 0.29 | 66 | 0.5\|0.0\|0.5 | 1.0 | 4.9 | 705 | 1380 | 0.22 |
| 3 | 1.0\|0.0\|0.0 | 1.5 | 8.5 | 1790 | 6440 | 0.34 | 67 | 0.5\|0.0\|0.5 | 1.5 | 5.8 | 1580 | 2300 | 0.26 |
| 4 | 1.0\|0.0\|0.0 | 2.0 | 9.9 | 3380 | 9710 | 0.37 | 68 | 0.5\|0.0\|0.5 | 2.0 | 6.7 | 2860 | 3420 | 0.29 |
| 5 | 1.0\|0.0\|0.0 | 3.0 | 12.3 | 8330 | 17100 | 0.42 | 69 | 0.5\|0.0\|0.5 | 3.0 | 8.3 | 6830 | 6300 | 0.34 |
| 6 | 1.0\|0.0\|0.0 | 6.0 | 17.5 | 36500 | 43200 | 0.49 | 70 | 0.5\|0.0\|0.5 | 6.0 | 11.7 | 29800 | 16200 | 0.42 |
| 7 | 1.0\|0.0\|0.0 | 12.0 | 22.6 | 134000 | 85300 | 0.54 | 71 | 0.5\|0.0\|0.5 | 12.0 | 15.1 | 110000 | 33800 | 0.49 |
| 8 | 1.0\|0.0\|0.0 | 20.0 | 28.1 | 353000 | 156000 | 0.60 | 72 | 0.5\|0.0\|0.5 | 20.0 | 18.7 | 299000 | 61000 | 0.50 |
| 9 | 0.0\|1.0\|0.0 | 0.5 | 3.4 | 179 | 409 | 0.14 | 73 | 0.3\|0.0\|0.7 | 0.5 | 3.4 | 159 | 451 | 0.12 |
| 10 | 0.0\|1.0\|0.0 | 1.0 | 4.0 | 689 | 733 | 0.18 | 74 | 0.3\|0.0\|0.7 | 1.0 | 4.3 | 607 | 977 | 0.20 |

(This table is available in its entirety in machine-readable form.)

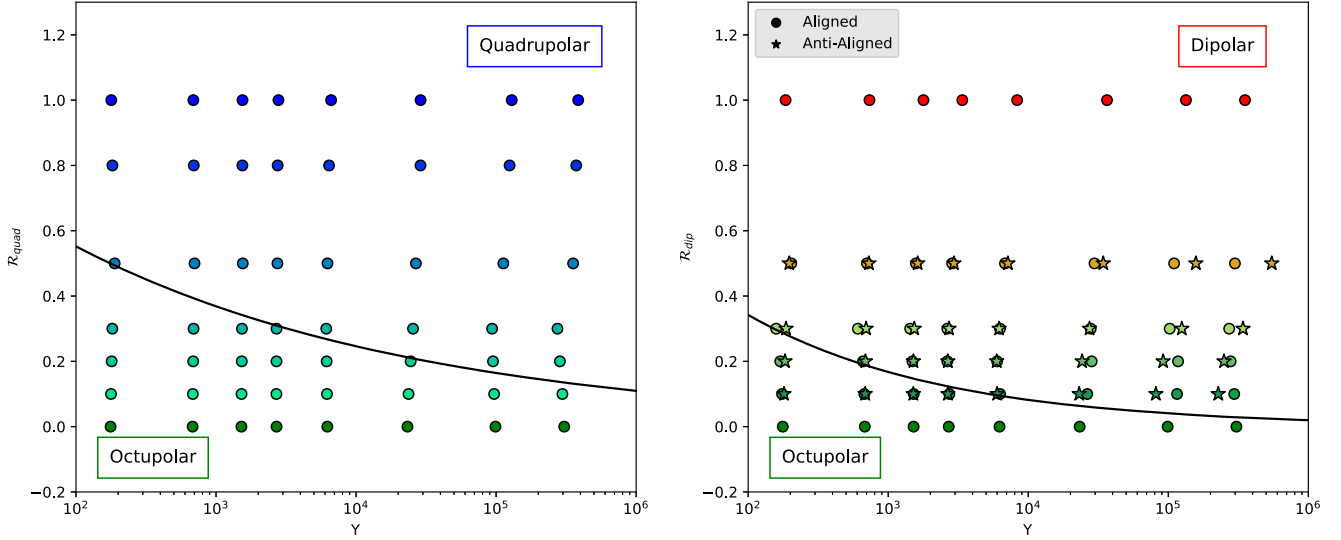**Figure 1.** The two parameter spaces first examined in this work, quadrupole–octupole (left) and dipole–octupole (right), shown in terms of $\Upsilon$ and either $\mathcal{R}_{quad}$ or $\mathcal{R}_{dip}$ (Equation (5)), respectively. Each point represents a simulation using the PLUTO code, with the color of each point labeling them throughout this work, depending on their relative combination of field components. The black solid lines represent $\Upsilon_{crit}$ for each combination, where the break in the Alfvén radius scaling is found (see equation (19)). In both two component parameter spaces, the average Alfvén radius scales as a pure octupole (bottom left) for low wind magnetisations and high octupole fraction. Then scales with the lowest-order component, either dipole or quadrupole (upper right).
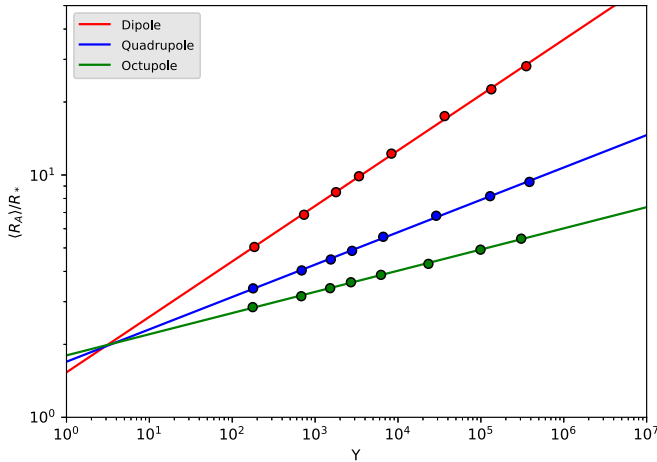


**Figure 2.** Average Alfvén radius vs. the wind magnetization, $\Upsilon$ (Equation (15)), in our simulations with single geometries (circles). Different scaling relations are shown for each pure geometry (solid lines). Higher $l$ order geometries produce a smaller Alfvén radius and thus smaller spin-down torque for a given polar field strength and mass-loss rate. A similar result was first shown by Réville et al. (2015).

rotation axis, $\langle R_A \rangle / R_* = (2/3)^{1/2}$ (Mestel 1968). Any significant magnetic braking in Sun-like stars will therefore be predominantly mediated by the lowest-order components.

### 3.2. Combined Magnetic Geometries

Based on work performed in Paper I, we anticipate the behavior of the average Alfvén radius for magnetic field geometries that contain, dipole, quadrupole, and octupole components. The dipole component, having the slowest radial decay, is expected to govern the field strength at large distances, then the field should scale like the quadrupole at intermediate distances, and finally, close to the star, the field should scale like the octupole geometry. The Alfvén radius formulation therefore takes the form of a twice-broken power
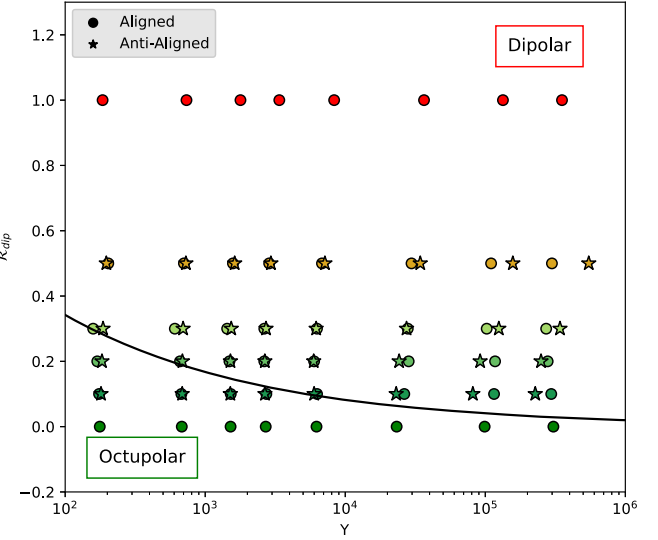
**Table 3**
Single Component Fit Parameters to Equation (16)

| Topology ($l$) | $K_s$ | $m_s$ |
|---|---|---|
| Dipole (1) | $1.53 \pm 0.03$ | $0.229 \pm 0.002$ |
| Quadrupole (2) | $1.70 \pm 0.02$ | $0.134 \pm 0.002$ |
| Octupole (3) | $1.80 \pm 0.01$ | $0.087 \pm 0.001$ |

**Note.** Fit values deviate slightly from those presented in Paper I owing to the more accurate numerical results found with logarithmic grid spacing, used here.

law,

$$\frac{\langle R_A \rangle}{R_*} = \max \begin{cases} K_{s,dip}[\mathcal{R}_{dip}^2 \Upsilon]^{m_{s,dip}}, \\ K_{s,quad}[(|\mathcal{R}_{dip}| + |\mathcal{R}_{quad}|)^2 \Upsilon]^{m_{s,quad}}, \\ K_{s,oct}[(|\mathcal{R}_{dip}| + |\mathcal{R}_{quad}| + |\mathcal{R}_{oct}|)^2 \Upsilon]^{m_{s,oct}}, \end{cases}$$
(17)

which approximates the simulated values of the average Alfvén radius. Note that $|\mathcal{R}_{dip}| + |\mathcal{R}_{quad}| + |\mathcal{R}_{oct}| = 1$, such that the final scaling depends purely on the total $\Upsilon$.

Here we present simulation results from combinations of each field, sampling a range of mixing fractions and field strengths. These are used to validate this semianalytic prescription for predicting the spin-down torque on a star, due to a given combination of axisymmetric magnetic fields.

#### 3.2.1. Dipole Combined with Quadrupole

The regime of dipole and quadrupole combined geometries is presented in Paper I. We briefly reiterate the results here, displaying values from that study in Figure 3.

These fields belong to different symmetry families, primary and secondary. As such, their addition creates a globally asymmetric field about the equator, with the north pole in this case being stronger than the south. The relative fraction of the two components alters the location of the current
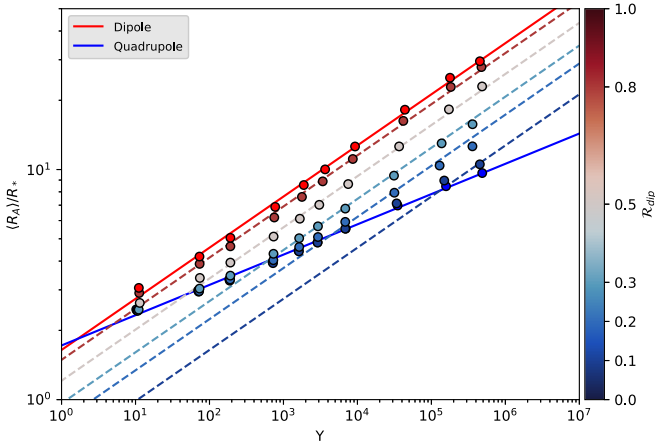
**Figure 3.** Average Alfvén radius scaling with wind magnetization, $\Upsilon$, for the different combinations of dipole and quadrupole, from the study in Paper I (circles). Solid lines show scaling for pure dipole and quadrupole. The deviation from single power laws shows how the combination of dipole and quadrupole fields modifies the Alfvén radius scaling, compared to single geometries. The scaling predicted by only considering the fractional dipole component is plotted with multiple dashed colored lines corresponding to the different $\mathcal{R}_{dip}$ values. This shows that $\langle R_A \rangle / R_*$ scales with the dipole component only, unless the quadrupole is dominant at a distance of $\approx R_A$.

sheet/streamers, which appear to resemble the dominant global geometry.

It is shown in Paper I that the quadrupole component has a faster radial decay than the dipole, and therefore at large distances only the dipole component of the field influences the location of the Alfvén radius. Closer to the star, the total field decays radially like the quadrupole, with the dipole component adding its strength, so near to the star the Alfvén radius scaling depends on the total field strength. Therefore, we developed a broken power law to describe the behavior of the average Alfvén radius scaling with wind magnetization, which uses the maximum of either the quadrupole slope using the total field strength, as if the combined field decays like a quadrupole (solid blue line), or the dipolar slope using only the dipole component (shown in color-coded dashed lines). The dipole component of the wind magnetization is formulated as

$$\Upsilon_{dip} = \left( \frac{B_*^{l=1}}{B_*} \right)^2 \frac{B_*^2 R_*^2}{\dot{M} v_{esc}} = \mathcal{R}_{dip}^2 \Upsilon. \tag{18}$$

Mathematically, Equation (17) becomes the broken power law from Paper I when $\mathcal{R}_{oct} = 0$,

$$\frac{\langle R_A \rangle}{R_*} = \begin{cases} K_{s,dip} [\mathcal{R}_{dip}^2 \Upsilon]^{m_{s,dip}}, & \text{if } \Upsilon > \Upsilon_{crit}(\mathcal{R}_{dip}), \\ K_{s,quad} [\Upsilon]^{m_{s,quad}}, & \text{if } \Upsilon \leqslant \Upsilon_{crit}(\mathcal{R}_{dip}), \end{cases} \tag{19}$$

where the octupolar relation is ignored, and $|\mathcal{R}_{dip}| + |\mathcal{R}_{quad}| = 1$. Here $\Upsilon_{crit}$ describes the intercept of the dipole component and quadrupole slopes,

$$\Upsilon_{crit}(\mathcal{R}_{dip}) = \left[ \frac{K_{s,dip}}{K_{s,quad}} \mathcal{R}_{dip}^{2m_{s,dip}} \right]^{\frac{1}{m_{s,quad}-m_{s,dip}}}. \tag{20}$$

Equation (17) further expands the reasoning above to include any field combination of the axisymmetric dipole, quadrupole, and octupole. The following sections test this formulation against simulated combined geometry winds.

### 3.2.2. Quadrupole Combined with Octupole

Stellar magnetic fields containing both a quadrupole and octupole field component present another example of primary and secondary family fields in combination. As with the axisymmetric dipole–quadrupole addition, the relative orientation of the two components simply determines which regions of magnetic field experience addition and subtraction about the equator, so that the torque and mass-loss rate do not depend on their relative orientation. Compared with the dipole component, both fields are less effective in generating a magnetic lever arm to brake rotation at a given value of $\Upsilon$.

We test the validity of Equation (17), setting $\mathcal{R}_{dip} = 0$ and systematically varying the value of $\mathcal{R}_{quad}$, with the octupole fraction composing the remaining field, $\mathcal{R}_{oct} = 1 - \mathcal{R}_{quad}$. Five mixed case values are selected ($\mathcal{R}_{quad} = 0.8, 0.5, 0.3, 0.2, 0.1$) that parameterize the mixing of the two geometries. Steady-state wind solutions are displayed in Figure 4, showing, as with dipole–quadrupole addition, the equatorially asymmetric fields produced. With increasing polar field strength, the streamers are observed to shift toward the lowest-order geometry morphology (quadrupolar in this case), as was shown for the dipole in Paper I.

The average Alfvén radii and wind magnetization are shown in Figure 5. The behavior of $\langle R_A \rangle$ is quantitatively similar to that of the dipole–quadrupole addition, where combined field cases are scattered between the two pure geometry scaling relations. The range of available $\langle R_A \rangle$ values between the pure quadrupole and octupole scaling relations (solid blue and green, respectively) is reduced compared to the previous dipole–quadrupole, due to the weaker dependence of the Alfvén radius with wind magnetization.

As required by Equation (17), with no dipolar component, we introduce the quadrupole component of $\Upsilon$ as

$$\Upsilon_{quad} = \left( \frac{B_*^{l=2}}{B_*} \right)^2 \frac{B_*^2 R_*^2}{\dot{M} v_{esc}} = \mathcal{R}_{quad}^2 \Upsilon, \tag{21}$$

and the second relation in Equation (17) takes the form

$$\frac{\langle R_A \rangle}{R_*} = K_{s,quad} [\Upsilon_{quad}]^{m_{s,quad}}, \tag{22}$$

where $K_{s,quad}$ and $m_{s,quad}$ are determined from the pure geometry scaling (see Table 3).

The quadrupole component of the wind magnetization is plotted for different $\mathcal{R}_{quad}$ values in Figure 5, showing an identical behavior to the dipole component in the dipole–quadrupole combined fields. The $\Upsilon_{quad}$ formulation is shown in Figure 6, with the solid blue line described by Equation (22). This agrees with a large proportion of the wind solutions, with deviations due to a switch of regime onto the octupole relation, the third relation in Equation (17),

$$\frac{\langle R_A \rangle}{R_*} = K_{s,oct} [\Upsilon]^{m_{s,oct}} = \frac{K_{s,oct}}{\mathcal{R}_{quad}^{2m_{s,oct}}} [\Upsilon_{quad}]^{m_{s,oct}}, \tag{23}$$

shown with a solid green line in Figure 5 and dashed color-coded lines in Figure 6. As with the dipole–quadrupole addition, a broken power law can be formulated taking the maximum of either the octupole scaling or the quadrupole component scaling, for a given $\mathcal{R}_{quad}$ value. For the cases simulated, we find a deviation from this broken power
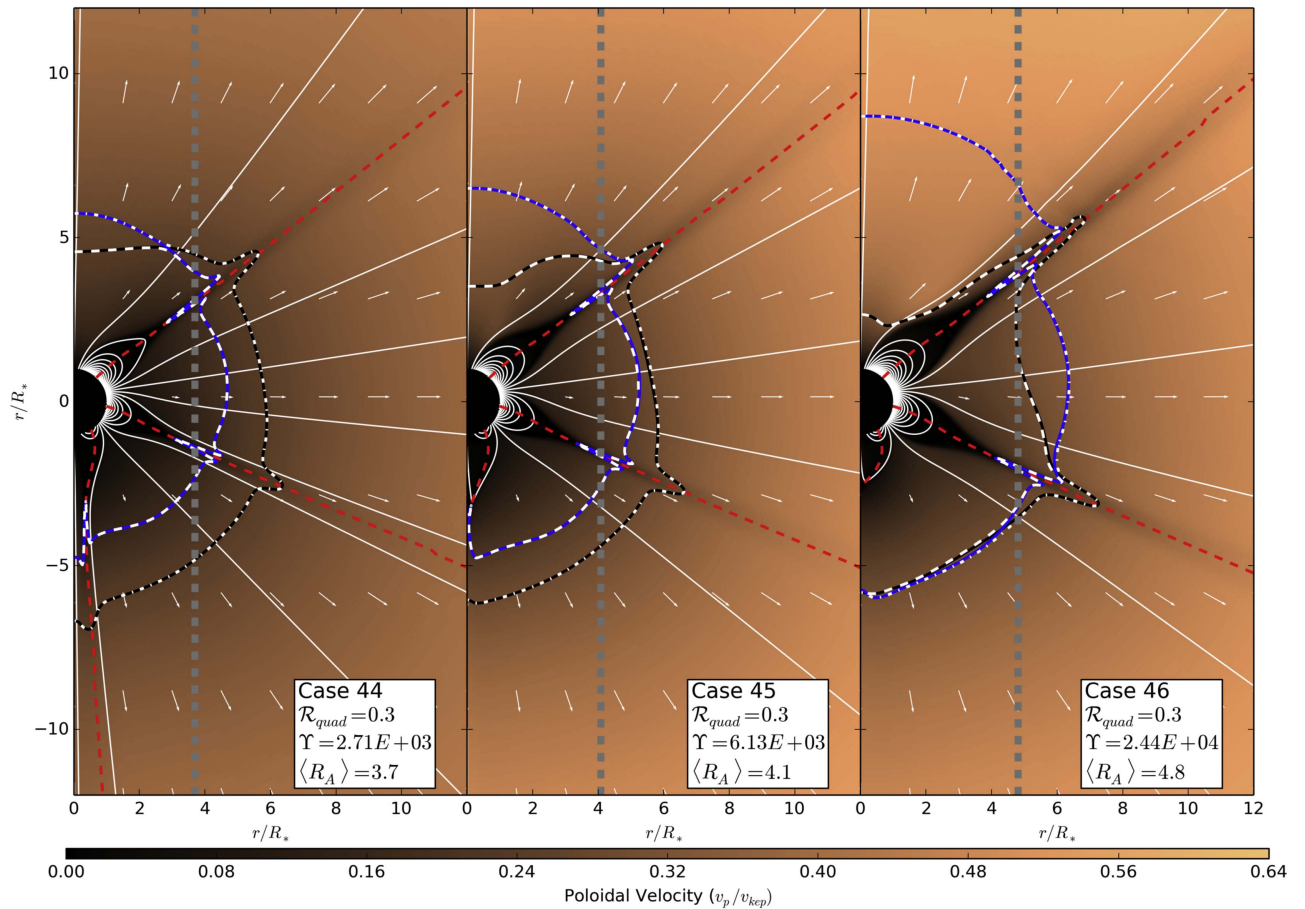
**Figure 4.** Steady-state solutions for the quadrupole–octupole combined geometry cases 44, 45, and 46, showing a progression from weaker to stronger magnetization ($\Upsilon$) from left to right. The color background represents the poloidal speed normalized by the Keplerian speed (e.g., $\approx$400 km s$^{-1}$ for solar parameters). Dead zones are therefore in black. Thin white lines trace the magnetic field, with red dashed lines highlighting the field polarity reversals (i.e., where $B_r = 0$). Alfvén and sonic surfaces are indicated with thick blue and black lines, respectively, with the fast and slow magnetosonic surfaces represented as dot-dashed and dashed white lines. Vertical gray dashed lines show the average Alfvén radius $\langle R_A \rangle$ (Equation (13), representing the torque efficiency, scales with the size of the Alfvén surface). The asymmetry of the global magnetic field about the equator is shown, with a qualitatively similar behavior to the dipole–quadrupole simulations in Paper I.

law of no greater than 5%, with most cases showing a closer agreement.

### 3.2.3. Dipole Combined with Octupole

Unlike the previous field combinations, both the dipole and octupole belong to the primary symmetry family, and thus their addition produces two distinct field topologies for aligned or anti-aligned fields. Again, we test Equation (17), now with $\mathcal{R}_{quad} = 0$. The field combinations are parameterized using the ratio of dipolar field to total field strength, $\mathcal{R}_{dip}$, with the remaining field in the octupolar component $\mathcal{R}_{oct} = 1 - \mathcal{R}_{dip}$. The ratio of dipolar field is varied ($\mathcal{R}_{dip} = 0.5, 0.3, 0.2, 0.1$). Additionally, we repeat these ratios for both aligned and anti-aligned fields. This produces eight distinct field geometries that cover a range of mixed dipole–octupole fields.

Figure 7 displays the behavior of both aligned and anti-aligned cases with increasing field strength. The combination of dipolar and octupolar fields produces a complex field topology that is alignment dependent and impacts the local flow properties of the stellar wind. The symmetric property of the global field is maintained about the equator. Aligned combinations have magnetic field addition over the poles, which increases the Alfvén speed, producing a larger Alfvén radius over the poles. However, the fields subtract over the

equator, which reduces the size of the Alfvén radius over the equator; see the top panel of Figure 4. The bottom panel shows anti-aligned mixed cases to exhibit the opposite behavior, with a larger equatorial Alfvén radius and a reduction to the size of the Alfvén surface at higher latitudes. The torque-averaged Alfvén radius is shown by the gray dashed lines in each case, representing the cylindrical Alfvén radius $\langle R_A \rangle$. For the simulations in this work, the anti-aligned cases produce a larger lever arm compared with their aligned counterparts, with a few exceptions. In general, the increased Alfvén radius at the equator for the anti-aligned fields is more effective at increasing the torque-averaged Alfvén radius compared with the larger high-latitude Alfvén radius in the aligned field cases.

The locations of the current sheets are shown in Figure 7 using red dashed lines. As noted with the dipole–quadrupole addition in Paper I, the global dipolar geometry is restored with increasing fractions of the dipole component or increased field strength for a given mixed geometry. The latter is shown in Figure 7 for both aligned and anti-aligned cases. With increased field strength, a single dipolar streamer begins to be recovered over the equator. A key difference between the two field alignments is the asymptotic location of the three streamers. In the case of an aligned octupole component, increasing the total field strength for a given ratio forces the streamers toward the equator, at which point they begin to
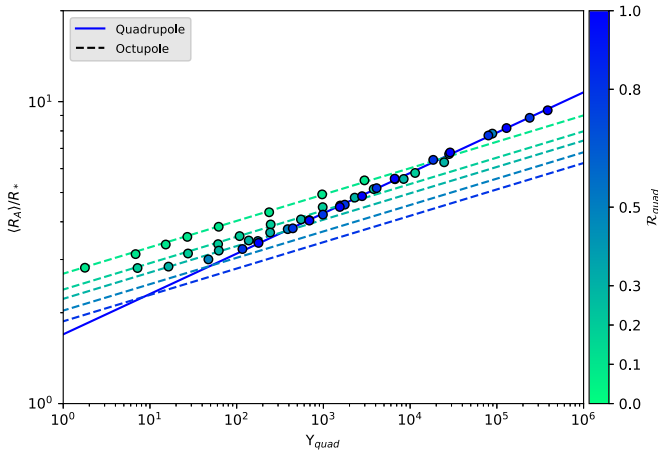
**Figure 5.** Average Alfvén radius vs. wind magnetization, $\Upsilon$, for the different combinations of quadrupole and octupole, in a similar format to Figure 3. Color-coded dashed lines relate to the prediction considering only the quadrupolar component of the field for each $\mathcal{R}_{quad}$. The combinations shown here behave in a similar manner to dipole–quadrupole combined fields, in a sense that the lower-order field (with the lowest $l$) governs the Alfvén radius for large wind magnetizations, $\Upsilon$, and the higher-order field (large $l$) controlling the low magnetization scaling.



**Figure 6.** Average Alfvén radius vs. the quadrupolar component of the wind magnetization, $\Upsilon_{quad}$, for cases with mixed quadrupole and octupole components (circles). The solid blue line shows the prediction based on the quadrupole component only (Equation (22)). The dashed lines show the octupolar scaling (Equation (23)). A broken power law composed of the quadrupolar component and the octupolar scaling ($\mathcal{R}_{quad}$ dependent) can be constructed similarly to work done in Paper I. The quadrupolar geometry dominates the scaling, for all of the $\mathcal{R}_{quad}$ values simulated here, at $\langle R_A \rangle / R_* \approx 9$. The point at which the quadrupolar geometry dominates for a given $\mathcal{R}_{quad}$ value can be approximated by considering the strength of the two fields at the Alfvén radii, i.e., the radial distance when the strength of the quadrupole matches or exceeds that of the octupole $B_{quad}/B_{oct} = \mathcal{R}_{quad}/(1 - \mathcal{R}_{quad})(r/R_*)$.

merge into the dipolar streamer. With an anti-aligned octupole component, the opposite is found, with the high-latitude streamers forced toward the poles and onto the rotation axis. It is unclear whether this effect is significant itself in influencing the global torque.

Using Equation (17), with no quadrupolar component, we anticipate that the dipolar component (first relation) will be the most significant in governing the global torque. Figures 8 and 9 show the dipole–octupole cases following the expected behavior, as observed for dipole–quadrupole and quadrupole–octupole combinations. We see that the average Alfvén radius follows either the dipole component scaling ($\Upsilon_{dip}$) or the octupole scaling relation,

$$\frac{\langle R_A \rangle}{R_*} = K_{s,oct}[\Upsilon]^{m_{s,oct}} = \frac{K_{s,oct}}{\mathcal{R}_{dip}^{2m_{s,oct}}}[\Upsilon_{dip}]^{m_{s,oct}}. \quad (24)$$

However, as evident in both figures, there is a deviation from this scaling, with the strongest variations belonging to low-$\mathcal{R}_{dip}$ cases. Anti-aligned cases follow the behavior expected from Paper I with a much higher precision than the anti-aligned cases. Figure 9 shows the dipole scaling to overpredict the aligned cases compared with the anti-aligned cases. This occurs because Equation (17) is a simplified picture of the actual dynamics within our simulations, and as such, it does not encapsulate all of the physical effects. The trends are still obvious for both aligned and anti-aligned cases, and the scatter simply represents a reduction to the precision of our formulation.

Despite this deviation from predicted values, Figure 9 shows the dipole component again to be the most significant in governing the global torque. With a more complex (higher $l$) secondary component, the dipole dominates the Alfvén radius scaling at a much lower wind magnetization, when compared with the dipole–quadrupole combinations. For the dipole–octupole cases simulated, the dipole component dominates the majority of the simulated cases. For our dipole and octupole mixed fields the transition between regimes occurs at
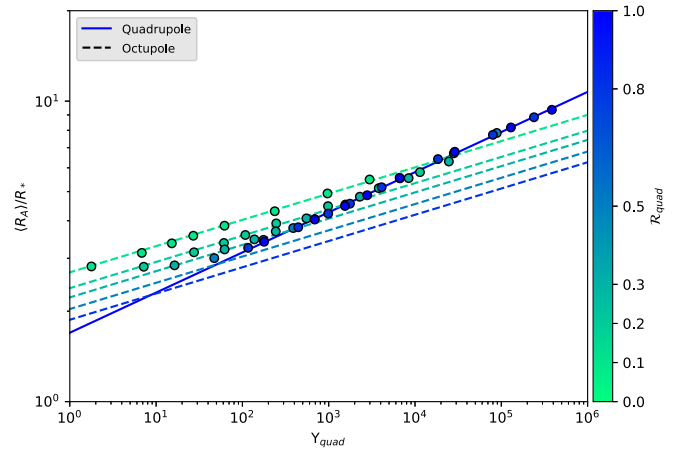
$\Upsilon_{dip} \approx 100$, such that the $\langle R_A \rangle$ for fields with $\mathcal{R}_{dip} = 0.1$, or higher, and a physically realistic wind magnetization will all be governed by the dipole component.

### 3.2.4. Combined Dipole, Quadrupole, and Octupole Fields

In addition to the quadrupole–octupole and dipole–octupole combinations presented previously, we also perform a small set of simulations containing all three components. Their stellar wind parameters and results are tabulated in Table 4. We select a regime where the dipole does not dominate ($\mathcal{R}_{dip} = 0.1$), to observe the interplay of the additional quadrupole and octupole components. We also utilize cases 89–96 and 121–128 from this work and cases 51–60 from Paper I, all of which sample varying fractions of quadrupole and octupole with a fixed $\mathcal{R}_{dip} = 0.1$. These are compared against the three-component cases, 129–160.

Equation (17) is adopted, now using all three components, such that the results from these simulations are expected to scale in magnetization like a twice-broken power law. As noted with the dipole–octupole addition, the inclusion of an octupolar component introduces behaviors that will not be accounted for by this formulation, i.e., Equation (17) is independent of field alignments, etc. We aim to characterize this unaccounted-for physics in terms of an available precision on the use of Equation (17). The simulated Alfvén radii are compared against their predicted values in Figure 10, along with the other simulations from this work (shown in white). The three-component field combinations have a small dipolar component; therefore, the dipolar scaling of the average Alfvén radius is rarely the dominant term in Equation (17). The different values of quadrupolar and octupolar field that compose the remaining field strength govern the average Alfvén radius scaling for the majority of this parameter space. From Figure 10, the approximate
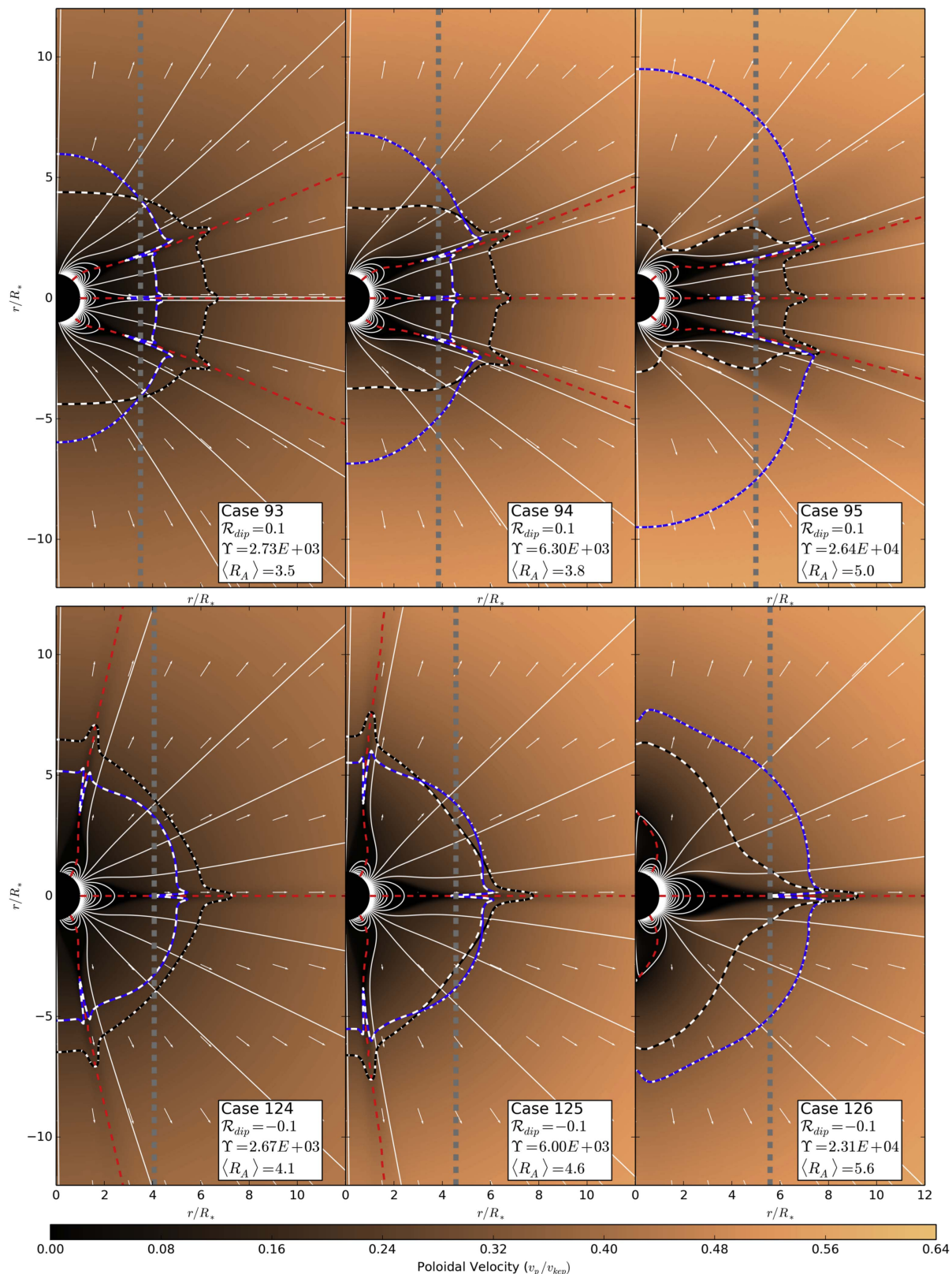
**Figure 7.** Steady-state solutions for the dipole–octupole combined geometries with aligned fields (top row; cases 93, 94, and 95) and anti-aligned fields (bottom row; cases 124, 125, and 126). The format and lines are the same as in Figure 4. The aligned cases have field adding near the poles and subtracting near the equator, where the opposite is true for the anti-aligned cases. The difference in how these two cases combine results in a different shape of the Alfvén surface. Also, for the same magnetization ($\Upsilon$), the anti-aligned cases, in general, systematically produce a larger torque efficiency ($\langle R_A \rangle$; vertical dashed gray lines). This is due to these cases having a stronger field at low latitudes, where the angular momentum loss is more efficient.
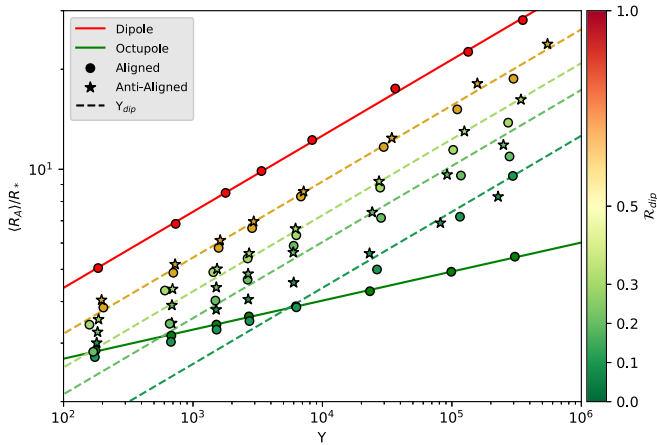
**Figure 8.** Average Alfvén radius scaling with wind magnetization, $\Upsilon$, for the different combinations of dipole and octupole. The fields are either added aligned at the poles (circles) or anti-aligned (stars). Dashed lines show the dipole component scaling, color-coded to match the simulated values of $\mathcal{R}_{dip}$. The overall behavior here is similar to the previous mixed combined fields, with the lower-order field governing the Alfvén radius for large wind magnetizations. However, the different field alignments appear to scatter around the $\Upsilon_{dip}$ approximation, with the anti-aligned cases typically having larger $R_A$ than the aligned cases, for the same $\Upsilon$.
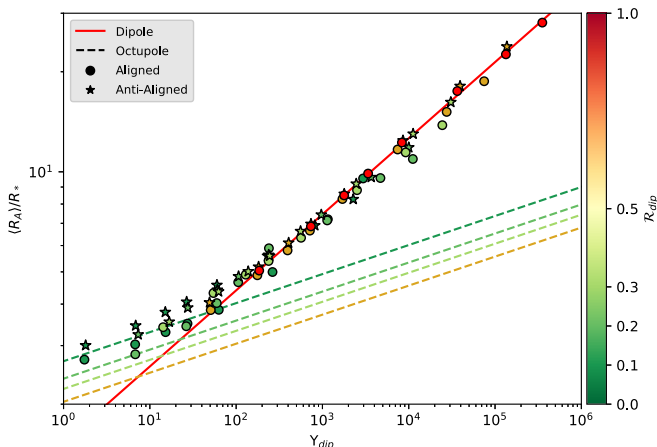


**Figure 9.** Average Alfvén radius scaling with only the dipolar component of the wind magnetization, $\Upsilon_{dip}$, for cases with combined dipole and octupole components. Aligned field are shown with circles, anti-aligned with stars. The parameter space investigated here is well approximated by the dipole component scaling relation (solid red line). Generally the aligned field cases are shown to undershoot the dipole component approximation, while the anti-aligned cases match the power law with similar agreement to the previous combined geometries. The qualitative behavior is again similar to the previous combined cases; however, due to the larger difference in radial decay of the field, i.e., $B_{dip}/B_{oct} = \mathcal{R}_{dip}/(1 - \mathcal{R}_{dip})(r/R_*)^2$, the dipole dominates at much smaller $R_A \approx 3$.

formulation agrees well with the simulated values, with the largest discrepancies emerging at smaller radii and for anti-aligned cases; see the residual plot below. A 10% divergence from our prediction (dashed lines in both the top and bottom panels of Figure 10) is shown to roughly approximate the effects not taken into account by the simple scaling, with the largest deviation to 18.3%.

Equation (17) is observed to have increasing accuracy as the Alfvén radii become larger in Figure 10; this is due to the increasing dominance of the dipolar component at large distances. Quantifying the scatter in our residual, we approximate the distribution of deviations as Gaussian and

calculate a standard deviation of 5.1%, when evaluating all 160 of our simulated cases. Considering the 32 three-component cases, the standard deviation remains of the same order of 5.2%, indicating that the formulation maintains precision with the inclusion of all three antisymmetric components. The largest deviations from the predicted values belong to the dipole–octupole simulations, and these are observed within Figures 8 and 9. In both figures, as well as the residual, the predicted values are shown to underestimate the simulated values, for small average Alfvén radii, but with increasing field strength they begin to overpredict. The trends in the residual represent physics not incorporated into our approximate formula and can be explained. The under-estimation at first is due to the sharpness of the regime transition from the broken-power-law representation; in reality, there is a smoother transition that is always larger than the break in power laws. This significantly impacts the dipole–octupole simulations, as they most often probe this regime, as can be seen within Figure 9. For the dipole–octupole combinations, we propose that this transition must be much broader to match the deviations in the residual of Figure 10.

Equation (17) represents an approximation to the impact of mixed geometry fields on the prediction of the average Alfvén radius. Our mixed cases are found to be well behaved and can all be predicted by this formulation within $\approx \pm 20\%$ accuracy for the most deviant; the majority lie within $\approx \pm 5\%$ accuracy.

### 3.3. Analysis of Previous Mixed Fields

Réville et al. (2015) presented mixed-field simulations containing axisymmetric dipole, quadrupole, and octupole components, based on observations of the Sun, at maximum and minimum of magnetic activity, along with a solar-like star TYC-0486. To further test our formulation, we use input parameters and results from Table 3 of Réville et al. (2015) and predict values for the average Alfvén radii of the mixed cases produced in their work. We use Equation (17) with the fit constants from their lower-temperature wind ($c_s/v_{esc} = 0.222$) and manipulate the given field strengths into suitable $\mathcal{R}_l$ values. Results can be found in Table 5 and are shown in Figure 10 with red squares. The predicted values for the Alfvén radii agree to better than 10% precision. The largest deviation, $\approx 8\%$, is for TYC-0486, which we credit to the location of the predicted Alfvén radius falling in between regimes, at the break in the power law (almost governed by the dipole component only), where the broken-power-law approximation has the biggest error.

Recent work by Réville & Brun (2017) presented 13 thermally driven wind simulations, in 3D, for the solar wind, using Wilcox Solar Observatory magnetograms, spanning the years 1989–2001. These simulations use the spherical harmonic coefficients derived from the magnetograms, up to $l = 15$, including the nonaxisymmetric modes. We predict the values of the average Alfvén radii using Equation (17), allowing the strength of any nonaxisymmetric component to be added in quadrature with the axisymmetric component to produce representative strengths for the dipole, quadrupole, and octupole components. For example, the dipole field strength is computed as

$$B_*^{l=1} = \sqrt{(B_{m=-1}^{l=1})^2 + (B_{m=0}^{l=1})^2 + (B_{m=1}^{l=1})^2}. \tag{25}$$

**Table 4**
Input Parameters and Results from Simulations with Three Magnetic Components

| Case | $\mathcal{R}_{dip}\|\mathcal{R}_{quad}\|\mathcal{R}_{oct}$ | $v_A/v_{esc}$ | $\langle R_A \rangle / R_*$ | $\Upsilon$ | $\Upsilon_{open}$ | $\langle v(R_A) \rangle / v_{esc}$ |
|---|---|---|---|---|---|---|
| 129 | 0.1\|0.6\|0.3 | 0.5 | 3.1 | 181 | 289 | 1.09 |
| 130 | 0.1\|0.6\|0.3 | 1.0 | 3.6 | 698 | 502 | 1.33 |
| 131 | 0.1\|0.6\|0.3 | 1.5 | 4.0 | 1550 | 709 | 1.49 |
| 132 | 0.1\|0.6\|0.3 | 2.0 | 4.4 | 2760 | 923 | 1.61 |
| 133 | 0.1\|0.6\|0.3 | 3.0 | 4.9 | 6320 | 1400 | 1.81 |
| 134 | 0.1\|0.6\|0.3 | 6.0 | 6.3 | 27100 | 3030 | 2.17 |
| 135 | 0.1\|0.6\|0.3 | 12.0 | 7.9 | 111000 | 6430 | 2.65 |
| 136 | 0.1\|0.6\|0.3 | 20.0 | 9.3 | 308000 | 11200 | 3.09 |
| 137 | 0.1\|0.6\|0.6 | 0.5 | 2.7 | 182 | 194 | 0.97 |
| 138 | 0.1\|0.3\|0.6 | 1.0 | 3.1 | 702 | 326 | 1.17 |
| 139 | 0.1\|0.3\|0.6 | 1.5 | 3.4 | 1560 | 451 | 1.29 |
| 140 | 0.1\|0.3\|0.6 | 2.0 | 3.7 | 2760 | 585 | 1.37 |
| 141 | 0.1\|0.3\|0.6 | 3.0 | 4.2 | 6230 | 903 | 1.53 |
| 142 | 0.1\|0.3\|0.6 | 6.0 | 5.5 | 25600 | 2180 | 1.85 |
| 143 | 0.1\|0.3\|0.6 | 12.0 | 7.2 | 97000 | 4850 | 2.25 |
| 144 | 0.1\|0.3\|0.6 | 20.0 | 8.6 | 246000 | 8560 | 2.61 |
| 145 | 0.1\|0.6\| − 0.3 | 0.5 | 3.2 | 34 | 312 | 1.13 |
| 146 | 0.1\|0.6\| − 0.3 | 1.0 | 3.7 | 119 | 533 | 1.37 |
| 147 | 0.1\|0.6\| − 0.3 | 1.5 | 4.1 | 258 | 765 | 1.53 |
| 148 | 0.1\|0.6\| − 0.3 | 2.0 | 4.5 | 451 | 1000 | 1.65 |
| 149 | 0.1\|0.6\| − 0.3 | 3.0 | 5.1 | 1020 | 1500 | 1.85 |
| 150 | 0.1\|0.6\| − 0.3 | 6.0 | 6.5 | 4450 | 3400 | 2.21 |
| 151 | 0.1\|0.6\| − 0.3 | 12.0 | 8.2 | 18600 | 7260 | 2.69 |
| 152 | 0.1\|0.6\| − 0.3 | 20.0 | 10.1 | 55300 | 13200 | 3.17 |
| 153 | 0.1\|0.3\| − 0.6 | 0.5 | 3.0 | 4 | 254 | 1.05 |
| 154 | 0.1\|0.3\| − 0.6 | 1.0 | 3.5 | 21 | 430 | 1.25 |
| 155 | 0.1\|0.3\| − 0.6 | 1.5 | 3.9 | 49 | 607 | 1.37 |
| 156 | 0.1\|0.3\| − 0.6 | 2.0 | 4.2 | 91 | 782 | 1.49 |
| 157 | 0.1\|0.3\| − 0.6 | 3.0 | 4.7 | 214 | 1160 | 1.65 |
| 158 | 0.1\|0.3\| − 0.6 | 6.0 | 5.9 | 916 | 2440 | 2.01 |
| 159 | 0.1\|0.3\| − 0.6 | 12.0 | 7.5 | 3770 | 5360 | 2.41 |
| 160 | 0.1\|0.3\| − 0.6 | 20.0 | 9.3 | 11300 | 10200 | 2.85 |

We obtained the field strengths for the dipole, quadrupole, and octupole components of the magnetograms used in the simulations of Réville & Brun (2017), ignoring the higher-order field components (V. Réville 2017, private communication). The results from this are shown in Figure 10 with magenta squares and show a good agreement in most cases to the simulated values. However, we note that the Alfvén radii tabulated within Réville & Brun (2017) are geometrically averaged rather than torque averaged, as used in this work (both scale with wind magnetization in a similar manner). These values thus represent the average spherical radius for the Alfvén surface in their 3D simulations. The base wind temperature for their simulations is also cooler ($c_s/v_{esc} \approx 0.234$) than in our simulations. Nevertheless, Figure 10 shows good agreement with the predicted values; we calculate a standard deviation of 8.4%. If we apply an approximate correction to the spherical radii with a factor of 2/3 (due to the angular momentum lever arm being proportional to $r \sin \theta$) and use torque scaling coefficients fit to the lower-temperature wind from Pantolmos & Matt (2017), we find that all the magenta simulations fit within the 10% precision, despite the inclusion of the nonaxisymmetric components. This suggests that Equation (17) can be used in cases with nonaxisymmetric geometries in combination, but further study is required to test more fully.

## 4. Analysis Based on Open Flux

### 4.1. Magnetic Flux Profiles

The behavior of the stellar wind torque, quantified in the previous sections, is similar to the results found in Paper I. Lower-order magnetic components decay more slowly with radius than higher-order components. Thus, the lower-order component typically dominates the dynamics of the global torque. The higher-order component can usually be ignored, unless it has a comparable field strength to the lower-order component at the Alfvén radius, which requires the higher-order field to dominate at the surface.

The radial dependence of the magnetic field is best described by the unsigned magnetic flux. To calculate this, we evaluate an integral of the magnetic field threading closed spherical shells with area $A$; this produces the unsigned magnetic flux as a function of radial distance,

$$\Phi(r) = \oint_r |\mathbf{B} \cdot d\mathbf{A}|. \tag{26}$$

For a potential field, as used in the initial conditions, the magnetic flux decays as a simple power law,

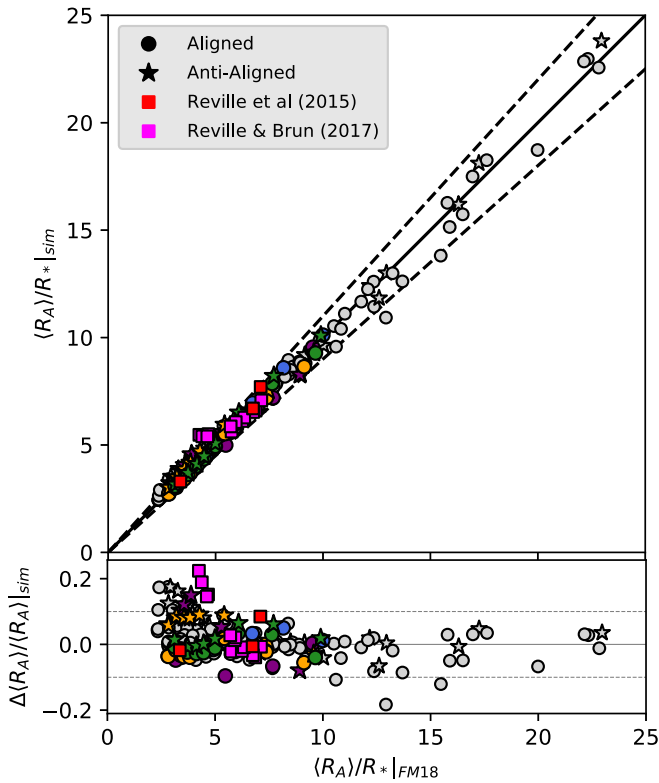$$\Phi(r) = \Phi_* \left( \frac{R_*}{r} \right)^l, \tag{27}$$

**Figure 10.** Top panel: comparison of the simulated Alfvén radii vs. the predicted Alfvén radii using Equation (17). The line of agreement is shown with a solid black line, and the bounds of 10% deviation from the predicted value are shown with black dashed lines. The bottom panel shows the residual, $(\langle R_A \rangle_{\rm sim} - \langle R_A \rangle_{\rm FM18})/\langle R_A \rangle_{\rm sim}$, and the 10% deviation with dashed lines. Cases 129–135 and 145–152 are colored purple, and cases 137–144 and 153–160 are colored orange, different from the color scheme of previous figures. The quadrupole- and octupole-dominated cases with $\mathcal{R}_{\rm dip} = 0.1$ are shown with their original coloring (blue and green, respectively). All other simulations from this work and Paper I are shown in gray. Three red squares represent axisymmetric mixed-field simulations from Réville et al. (2015). Thirteen magenta squares represent 3D nonaxisymmetric simulations with $l_{\rm max} = 15$ from Réville & Brun (2017) (the average Alfvén radius is computed differently than Equation (13)).

**Table 5**
Comparison of Results, $R_A/R_*|_{\rm sim}$, from Cases of Réville et al. (2015)
to the Prediction of Equation (17), $R_A/R_*|_{\rm FM18}$

| Object | $\mathcal{R}_{\rm dip}|\mathcal{R}_{\rm quad}|\mathcal{R}_{\rm oct}$ | $\Upsilon$ | $R_A/R_*|_{\rm sim}$ | $R_A/R_*|_{\rm FM18}$ |
|---|---|---|---|---|
| Sun Min | $-0.47|0.03| - 0.50$ | 812 | 6.7 | 6.74 |
| Sun Max | $0.13|0.73|0.14$ | 130 | 3.3 | 3.36 |
| TYC-0486 | $-0.10|0.79| - 0.11$ | 17600 | 7.7 | 7.10 |

where $\Phi_*$ is the surface magnetic flux and $l$ represents the magnetic order of the field, increasing for more complex fields. Thus, higher-order fields decay radially faster.

The radial profiles of the flux in our steady-state solutions are shown with thin gray lines in Figures 11–13. Each ratio ($\mathcal{R}_l$) represents a different combined field geometry, with each gray line having a different field strength. In each figure we include the potential field solution for the flux with a solid black line, produced by Equation (26), showing the initial magnetic field configuration. No longer is a single power law produced; instead, the components interact and produce a varying radial decay. In magnetized winds, the magnetic forces balance the thermal and ram pressures close to the star. Therefore, the

unsigned flux approximately follows the potential solution. Farther from the star the pressure of the wind forces the magnetic field into a nearly radial configuration, beyond which the unsigned flux becomes constant. This constant value is referred to as the open flux, $\Phi_{\rm open}$ (typically larger field strength produces a smaller fraction of open flux to surface flux).

In the cases with quadrupole–octupole mixed fields (Figure 11), the individual potential field quadrupole and octupole components are indicated with thick dashed blue and green lines, respectively. As with the previous dipole and quadrupole addition, the broken-power-law behavior shown in the Alfvén radius formulation is visible. The quadrupole component often represents the most significant contribution to the total flux, as the dipole did within Paper I. The bottom right panel of Figure 11 shows the relative decay of all the potential fields.

Figure 12 shows the radial magnetic flux evolution for the dipole–octupole combinations in a similar format to Figure 11. A quantitatively similar behavior to the dipole–quadrupole and quadrupole–octupole combinations is shown with the anti-aligned field geometries, seen in the bottom row. This explains why previously the anti-aligned cases provided a better fit to the broken-power-law approximation than the aligned cases. For the cases with an aligned octupole component, the profile of the flux decay is distinctly different. The smooth transition between the two regimes of the broken power law is replaced with a deviation from the dipole that passes below the dipole component at first and then asymptotes back. This is caused by the subtraction of the dipole and octupole fields over the equator, which reduces the unsigned flux and has the largest impact at the radial distance where the two components have the equal and opposite field strength.

For these two-component simulations, the approximate formulation, Equation (17), mathematically approximates the radial decay of the magnetic field with two regimes, an octupolar decay close in to the star followed by a sharp transition to the lower-order geometry (dipole or quadrupole), which ignores any influence of the octupolar field. The formulation works well when this is a good approximation, which is typically the case for the dipole–quadrupole, quadrupole–octupole, and anti-aligned dipole–octupole cases. The inflection of the magnetic flux for aligned cases creates a discrepancy between our simplification and the physics in the simulation; therefore, we observe a scatter in our results between the aligned and anti-aligned cases. Our formulation is least precise when the inflection occurs near the Alfvén radius, causing the formula to overpredict the average Alfvén radius. However, in Section 3.2.4 we show this to be a systematic and measurable effect that does not impact the validity of Equation (17).

For the three-component simulations, the behavior of the dipole-octupolar component alignment is shown to oppose the previous dipole–octupole addition. Equation (17) more accurately approximates the mixed-field cases with an aligned octupole component than with an anti-aligned component. To explore this, we show the radial evolution of the magnetic flux in Figure 13. The top panel displays the aligned cases with increasing octupolar component and decreasing quadrupolar component, moving to the right. The reduction of flux, or inflection in the flux profile, due to the dipole and octupole addition is only seen to be significant for one case, where the octupole fraction is maximized. In the remaining cases the
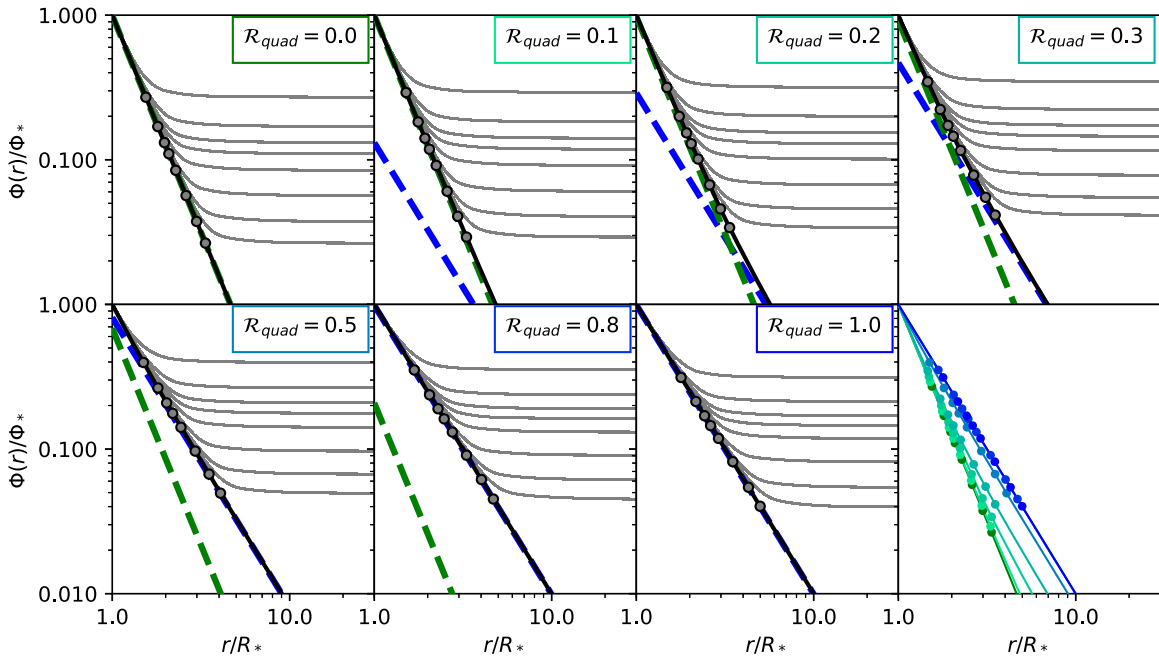
**Figure 11.** Unsigned magnetic flux vs. radial distance (gray lines) for all the cases with combined quadrupole and octupole components (labeled $\mathcal{R}_{quad} = 0.1 - 0.8$, along with the pure quadrupole and octupole cases (labeled $\mathcal{R}_{quad} = 0.0$ and $1.0$). Thick dashed blue and green lines show the value for a potential field for the quadrupole and octupole components, respectively, on their own. The total potential field flux, used as the initial condition, Equation (26), is shown in solid black. Thin gray lines in each panel show the magnetic flux in a single steady-state solution, for different field strengths of a given geometry. The flux within the simulations follows the potential field solution closely until the magnetic field is opened into a radial configuration with constant flux. Gray circles indicate the location of the field opening radii $R_o$, as we define it in this work. The mixed field geometries decay with an octupolar dependence until reaching the quadrupolar component, at which point the quadrupole controls the decay. This explains why the broken-power-law approximation is a good fit to the data in most cases. For comparison, the final panel shows all of the potential (initial) field geometries and their opening radii, colored according to their $\mathcal{R}_{quad}$ value.

octupolar fraction is too small to produce a strong reduction in the equatorial flux with the dipole, hence the well-behaved relation between the simulated aligned cases and the predicted average Alfvén radii in Figure 10. The poorest-fitting cases to Equation (17) are the anti-aligned mixed cases shown in Figure 13 with purple and orange stars. The potential field solutions, shown with solid black lines, sit above the dashed component slopes (most significant for cases 153–160, in orange) showing an increased field strength due to the complex addition of the three components in combination. This is unlike most of the previous combined field cases, which are typically described by either one component or the other; hence, the predicted values differ for these cases.

This behavior is difficult to parameterize within our Alfvén radius approximation, as it requires knowledge about the magnetic field evolution in the wind. For this work, we simply show why the simulations deviate from Equation (17) and suggest that care be taken when using such formulations with dipolar and octupolar components.

### 4.2. Open Flux Torque Relation

The open flux, $\Phi_{open}$, remains a key parameter in describing the torque scaling for any magnetic geometry. Réville et al. (2015) construct a semianalytic formulation for the average Alfvén radius using the open flux wind magnetization,

$$\Upsilon_{open} = \frac{\Phi_{open}^2 / R_*^2}{\dot{M} v_{esc}}. \qquad (28)$$

The dependence of the average Alfvén radius on $\Upsilon_{open}$ is then parameterized:

$$\frac{\langle R_A \rangle}{R_*} = K_o [\Upsilon_{open}]^{m_o}, \qquad (29)$$

where $K_o$ and $m_o$ represent fit parameters to our simulations using this open flux formulation. In Paper I, we show the dependence of these fit parameters on magnetic geometry. We show this again within the left panel of Figure 14. The scatter in average Alfvén radius values for different field geometries is reduced compared with that seen in the $\Upsilon$ parameter spaces (Figures 3, 5, and 8), such that a single power-law fit is viable, shown with a solid black line. However, better fits are obtained when considering each pure geometry independently, tabulated in Table 6.

Work by Pantolmos & Matt (2017) showed how differing wind acceleration affects the scaling relation by using different base wind temperatures to accelerate their winds. Different magnetic topologies produce slightly different wind acceleration from the stellar surface out to the Alfvén radius, due to the varying degree of super-radial expansion of the magnetic field lines (Velli 2010; Riley & Luhmann 2012; Réville et al. 2016). Thus, this causes the distinctly different scaling relations in the left panel of Figure 14. Using the averaged Alfvén speed $\langle v(R_A) \rangle$ at the Alfvén surface, this difference in wind acceleration can be removed (see Pantolmos & Matt 2017), and the result is shown in the right panel of Figure 14.
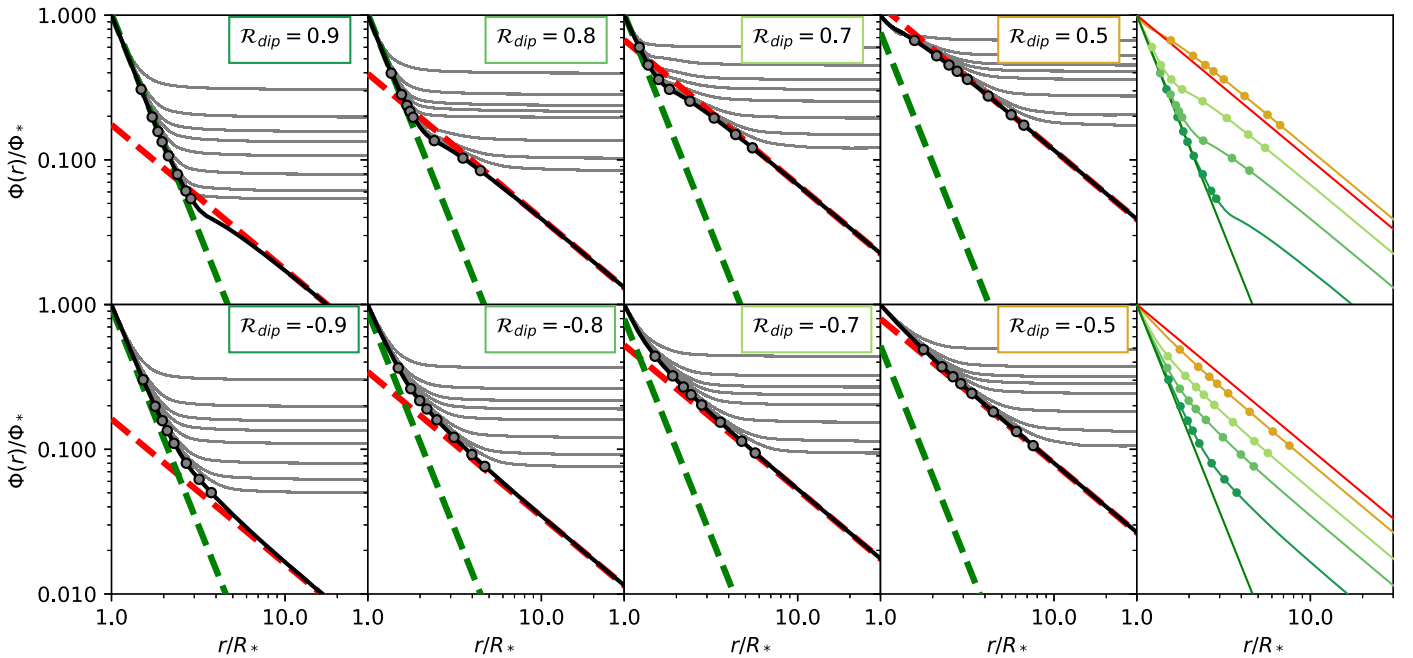
**Figure 12.** Unsigned magnetic flux vs. radial distance for all the cases with combined dipole and octupole components (labeled $\mathcal{R}_{dip} = \pm 0.5$–$0.9$), both aligned (top row) and anti-aligned (bottom row), in a similar format to Figure 11. Thick dashed red and green lines show the value for a potential field for the dipole and octupole components, respectively, on their own. The aligned cases have a qualitatively different behavior from the dipole–quadrupole, quadrupole–octupole, and anti-aligned dipole–octupole cases, in that the former show a subtle inflection in their flux vs. radius (most apparent in the solid black lines for large $\mathcal{R}_{dip}$ values, the three top left panels). This is caused by the subtraction of the two fields in the equatorial region, which has a maximum effect at the radius where the two components have the same magnitude. The net effect of this inflection in the magnetic flux is subtle, and thus our scaling relation (which does not treat the aligned and anti-aligned cases differently) remains an acceptable approximation to all simulations. For comparison, the rightmost panel shows all of the potential (initial) field geometries and their opening radii, colored according to their $\mathcal{R}_{dip}$ value, for the aligned and anti-aligned cases, respectively.

The semianalytic solution from Pantolmos & Matt (2017) is given by

$$\frac{\langle R_A \rangle}{R_*} = K_c \left[ \Upsilon_{open} \frac{v_{esc}}{\langle v(R_A) \rangle} \right]^{m_c}, \qquad (30)$$

where $K_c$ and $m_c$ are fit parameters to this formulation. The fit relationship from Pantolmos & Matt (2017) and a fit to our simulation data (Table 6) are shown with all our simulated cases (both Paper I and this paper) in the right panel of Figure 14.

A small geometry-dependent scatter remains in the right panel, which is noted in Paper I. The cause of this is an unanswered question but may relate to systematic numerical errors due to modeling small-scale complex field geometries. Our fit agrees well with that from Pantolmos & Matt (2017), with a shallower slope due to the inclusion of the higher-order geometries that show this systematic deviation from the dipole simulations.

### 4.3. Field Opening Radius

As in previous works (e.g., Pantolmos & Matt 2017; Paper I), we define an opening radius $R_o$ using the value of the open flux. The opening radius is defined as the radial distance at which the potential field for a given geometry matches the value of the open flux, i.e., $\Phi(R_o) = \Phi_{open}$. In this way, given the surface magnetic field geometry and the value of $R_o$, the open flux in the wind is recovered, and thus the torque can be predicted. However, producing a single relation

for predicting the opening radius, and thus the open flux, for our simulations remains an unsolved problem.

In Figures 11–13, the opening radii for all simulations are marked with gray circles and compared in the final panel (colored to match the respective $\mathcal{R}_l$ value). With increasing field strength, the simulations produce a larger average Alfvén radius and a larger dead zone/opening radius. The Alfvén and opening radii roughly grow together with increasing wind magnetization, but their actual behavior is more complex. The field complexity also has an affect on this relationship, with more complex geometries producing smaller opening radii, as the wind pressure is able to open the magnetic field closer to the star.

We compare the average Alfvén radii and opening radii within Figure 15. The simulations containing an octupolar component, in general, show a shallower dependence, which continues the trend from dipole to quadrupole presented in Paper I. Interestingly, the aligned dipole–octupole fields are shown to have reduced values of $R_o$ for the Alfvén radii they produce, compared to the aligned cases, which is a consequence of the reduced flux from the field subtraction over the equator. For these cases the wind pressure is able to open the field much closer to the star, compared to the anti-aligned cases.

The relationship between the opening radius and the lever arm for magnetic braking torque in our wind simulations is evidently complex and interrelated with magnetic geometry, field strength, and mass-loss rate. The opening radius, as we define it here, is algebraically related to the source surface radius, $r_{ss}$, used within the potential field source surface (PFSS) models. As such, the $R_o$ scales with $r_{ss}$ for a given field
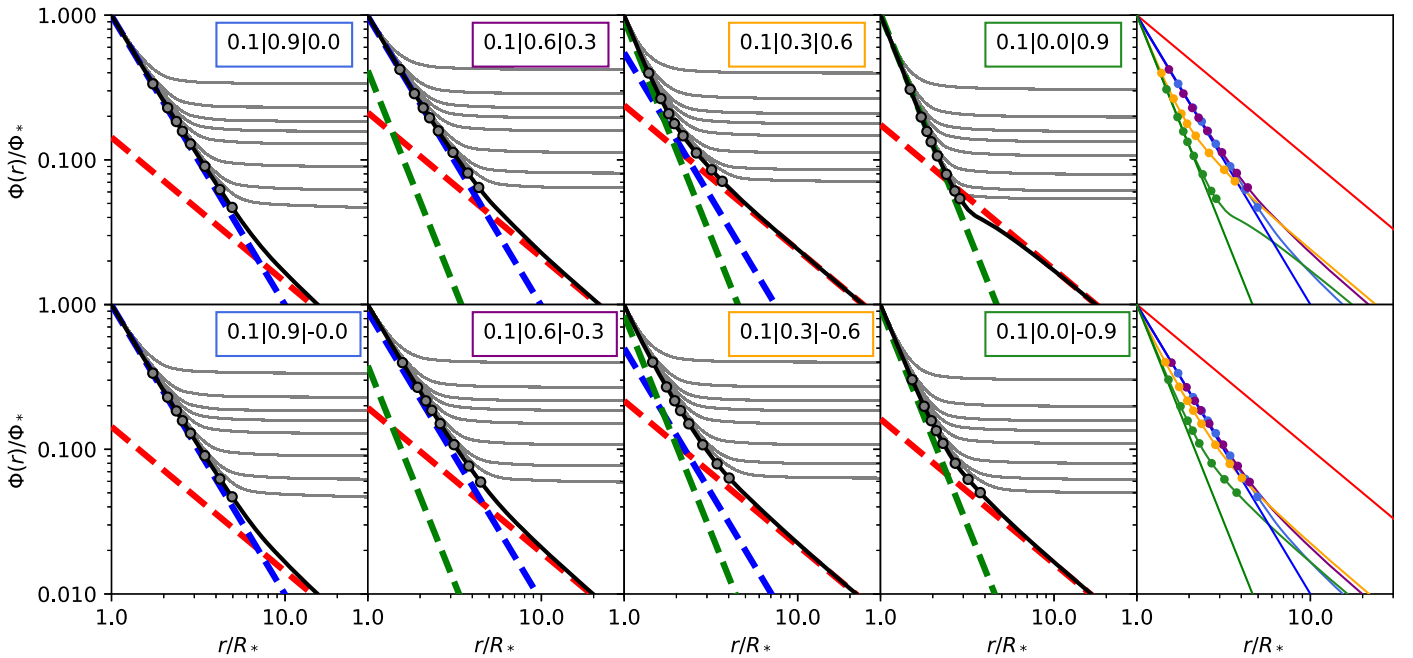
**Figure 13.** Unsigned magnetic flux vs. radial distance for the sample of mixed dipole, quadrupole, and octupole cases in the same format as Figure 11. All cases shown have 10% in the dipole component. Then, from left to right, the fraction in the octupole increases from 0% to 90% (with the remaining fraction in the quadrupole component). The top row has aligned dipole–octupole; the bottom has anti-aligned.
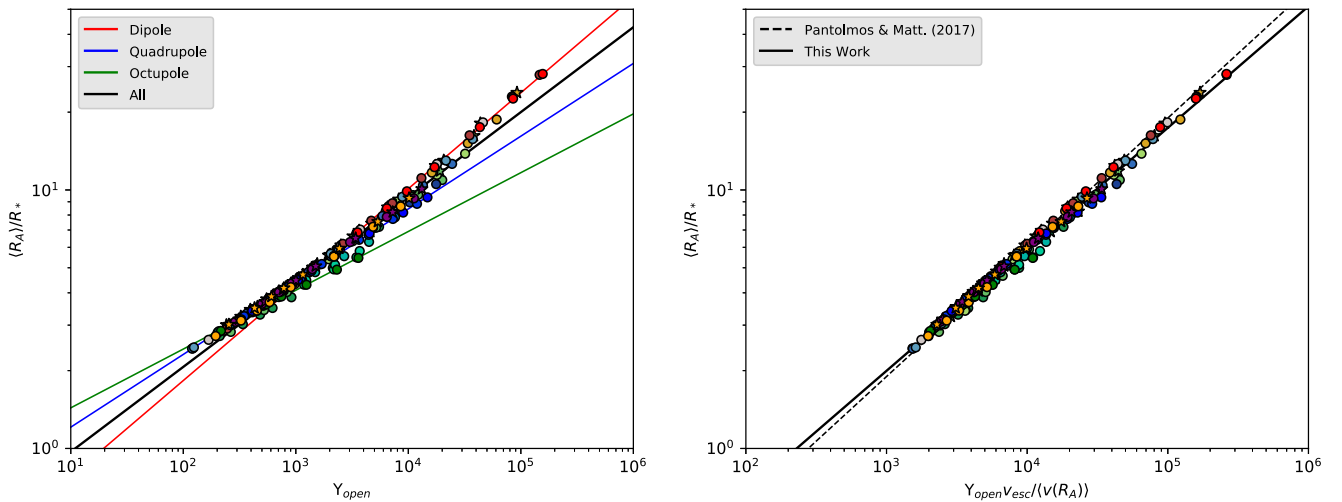


**Figure 14.** Average Alfvén radius vs. the open flux magnetization, $\Upsilon_{\rm open}$, Equation (28). All simulations from this study and Paper I are shown, color-coded as in the previous figures. Left: different scaling relations (Equation (29), Table 6) are shown for each pure geometry and a combined fit. Right: open flux magnetization divided by the average speed at the Alfvén surface $\langle v(R_A) \rangle$. The scatter is reduced, indicating that the different scalings in the left panel are primarily due to the effect of magnetic geometry on the wind acceleration (as discussed in Paper I). However, there remains a small systematic trend, in that the higher-order geometry winds sit lower for a given magnetization (seen in Paper I), which may be due to systematic numerical effects. The solid black line represents the fit to all data (see Table 6); the dashed line represents the result from dipole wind simulations with different base wind temperatures from Pantolmos & Matt (2017).

geometry, and its behavior with increasing field strength should be accounted for within future PFSS models.

## 5. Conclusions

This work presents results from 160 new MHD simulations and 50 previously discussed simulations from Paper I, which we use to disentangle the impacts of complex magnetic field geometries on the spin-down torque produced by magnetized stellar winds. Axisymmetric dipole, quadrupole, and octupole fields are used to construct differing combined field geometries.

We systematically vary the ratios, $\mathcal{R}_{\rm dip}$, $\mathcal{R}_{\rm quad}$, and $\mathcal{R}_{\rm oct}$, of each field geometry with a range of total field strengths. Here we reinforce results from Paper I. With simple estimates using realistic magnetic field topologies (obtained from ZDI observations) and representative field strengths and mass-loss rates for main-sequence stars, the dipole component dominates the spin-down process, irrespective of the higher-order components (A. Finley et al. 2018, in preparation). The original formulation from Matt et al. (2012) remains robust in most cases even for significantly nondipolar fields. Combined with the work from Pantolmos & Matt (2017), these formulations represent a strong
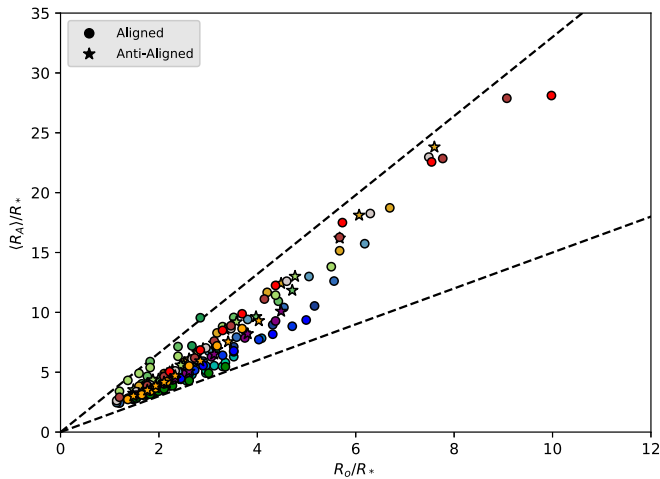
**Figure 15.** Average Alfvén radius vs. opening radius for all cases. Black dashed lines represent $R_A/R_o = 3.3$ and 1.5, which bound all cases. The simulations show a similar behavior to that discussed in Paper I, namely, a geometry-dependent separation, with the octupole geometries having the shallowest slope.

**Table 6**
Open Flux Fit Parameters to Equations (29) and (30)

| Topology($l$) | $K_o$ | $m_o$ |
|---|---|---|
| Dipole (1) | $0.33 \pm 0.03$ | $0.371 \pm 0.003$ |
| Quadrupole (2) | $0.63 \pm 0.02$ | $0.281 \pm 0.003$ |
| Octupole (3) | $0.85 \pm 0.03$ | $0.227 \pm 0.004$ |
| All simulations | $0.46 \pm 0.03$ | $0.329 \pm 0.004$ |
| | $K_c$ | $m_c$ |
| Topology independent | $0.08 \pm 0.04$ | $0.470 \pm 0.004$ |

foundation for predicting the stellar wind torques from a variety of cool stars with differing properties.

We show the distinctly different changes to topology from our combined primary (dipole, octupole) and secondary (quadrupole) symmetry family fields, "primary" being anti-symmetric about the equator and "secondary" symmetric about the equator (McFadden et al. 1991; DeRosa et al. 2012). The addition of primary and secondary fields produces an asymmetric field about the stellar equator, in contrast to the combination of two primary fields, which maintains equatorial symmetry. However, the latter case breaks the degeneracy of the field alignment, producing two different topologies dependent on the relative orientation of the combined geometries. This is not the case for primary and secondary field addition, i.e., dipole–quadrupole and quadrupole–octupole, which produces the same global field reflected about the equator.

The magnetic braking torque is shown, as in Paper I, to be largely dependent on the dominant lowest-order field component. For observed field geometries this is, in general, dipolar in nature. We parameterize the torque from our mixed-field simulations based on the decay of the magnetic field. The average Alfvén radius, $\langle R_A \rangle$, is defined to represent a lever arm, or efficiency factor, for the torque, Equation (14). From our simulated cases we produce an approximate formulation for the average Alfvén radius, Equation (17), where both $K_s$ and $m_s$ have tabulated values from our simulations in Table 3. These values are temperature dependent, e.g., $\approx 1.7$ MK for a $1 M_\odot$ star. In this formulation, the octupole geometry dominates the magnetic field close to the star; then it decays radially, leaving the quadrupole governing the radial decay of the field; and finally the quadrupole decays, leaving only the dipole component of the field. In each regime the strength of the field includes any component that is yet to decay away.

Using this formula, we are able to predict the torque in all of our simulations to $\approx 20\%$ accuracy, with the majority predicted to within $\approx 5\%$. This is then extended to mixed-field simulations presented in Réville et al. (2015) and Réville & Brun (2017). The formulation presented within this work remains an approximation, with a smoother transition from each regime observed with the simulations. This work

represents a modification to existing torque formulations, which accounts for combined field geometries in a very general way. A key finding remains that the dipole component is able to account for the majority of the magnetic braking torque, in most cases. Thus, previous works based on the assumption of the dipolar component being representative of the global field are validated. It is noted here, however, that it is the dipole component of the field and not the total field strength that enters in the torque formulation; therefore, it is important to decompose any observed field correctly to avoid miscalculation.

In this study, as in the previous one, we do not include the effects of rapid rotation or varying coronal temperatures. Prescriptions for rotational effects on the three pure geometries studied here are available (Matt et al. 2012; Réville et al. 2015), along with differing coronal temperatures for dipolar geometries (Pantolmos & Matt 2017). In general, differences in wind-driving parameters and physics will introduce more deviation from Equation (17); however, it is expected to remain valid.

Work remains in modeling the behavior of nonaxisymmetric components on the stellar wind environments surrounding Sun-like and low-mass stars and the associated spin-down torques. Observed fields are shown to host a varied amount of nonaxisymmetry (e.g., See et al. 2015). Works including more complex coronal magnetic fields, such as the inclusion of magnetic spots (e.g., Cohen et al. 2009; Garraffo et al. 2015), tilted magnetospheres (e.g., Vidotto et al. 2010), and using ZDI observations (e.g., Vidotto et al. 2011, 2014; Alvarado-Gómez et al. 2016; Garraffo et al. 2016b; Nicholson et al. 2016; Réville et al. 2016), have shown the impact of specific cases but have yet to fully parameterize the variety of potential magnetic geometries. The relative orientations of some field combinations shown in this work have produced differences in the braking lever arm; therefore, we expect the same to be true for nonaxisymmetric geometries in combination. Since Equation (17) predicts the Alfvén radii from Réville & Brun (2017) (Section 3.3), this suggests that our approximate formulation holds for nonaxisymmetric components (using a quadrature addition of $\pm l$ components), but this remains to be validated.

*Software:* matplotlib (Hunter 2007), PLUTO (Mignone et al. 2007; Mignone 2009).

## ORCID iDs

Adam J. Finley ◉ https://orcid.org/0000-0002-3020-9409
Sean P. Matt ◉ https://orcid.org/0000-0001-9590-2274

## References

Agüeros, M. A., Covey, K. R., Lemonias, J. J., et al. 2011, ApJ, 740, 110
Alvarado-Gómez, J., Hussain, G., Cohen, O., et al. 2016, A&A, 594, A95
Amard, L., Palacios, A., Charbonnel, C., Gallet, F., & Bouvier, J. 2016, A&A, 587, A105
Aschwanden, M. 2006, Physics of the Solar Corona: An Introduction with Problems and Solutions (2nd ed.; Berlin: Springer)
Barnes, S. A. 2003, ApJ, 586, 464
Barnes, S. A. 2010, ApJ, 722, 222
Blackman, E. G., & Owen, J. E. 2016, MNRAS, 458, 1548
Bouvier, J., Matt, S. P., Mohanty, S., et al. 2014, in Protostars and Planets VI, ed. H. Beuther et al. (Tucson, AZ: Univ. Arizona Press), 433
Brown, T. M. 2014, ApJ, 789, 101
Brun, A. S., & Browning, M. K. 2017, LRSP, 14, 4
Brun, A. S., Petit, P., Jardine, M., & Spruit, H. C. 2013, in IAU Symp. 302, Magnetic Fields throughout Stellar Evolution, ed. P. Petit et al. (Cambridge: Cambridge Univ. Press), 114
Cohen, O., Drake, J., Kashyap, V., & Gombosi, T. 2009, ApJ, 699, 1501
Cohen, O., Kashyap, V., Drake, J., et al. 2011, ApJ, 733, 67
Cranmer, S., & Van Ballegooijen, A. 2005, ApJS, 156, 265
Cranmer, S. R., Gibson, S. E., & Riley, P. 2017, SSRv, 212, 1345
Cranmer, S. R., Van Ballegooijen, A. A., & Edgar, R. J. 2007, ApJS, 171, 520
Davenport, J. R. A. 2017, ApJ, 835, 16
Delorme, P., Cameron, A. C., Hebb, L., et al. 2011, MNRAS, 413, 2218
DeRosa, M., Brun, A., & Hoeksema, J. 2012, ApJ, 757, 96
do Nascimento, J.-D., Jr, Vidotto, A., Petit, P., et al. 2016, ApJL, 820, L15
Donati, J.-F., Forveille, T., Cameron, A. C., et al. 2006, Sci, 311, 633
Donati, J.-F., Jardine, M., Gregory, S., et al. 2007, MNRAS, 380, 1297
Donati, J.-F., Moutou, C., Fares, R., et al. 2008, MNRAS, 385, 1179
Fares, R., Donati, J.-F., Moutou, C., et al. 2009, MNRAS, 398, 1383
Feldman, U., Landi, E., & Schwadron, N. 2005, JGRA, 110, A07109
Finley, A. J., & Matt, S. P. 2017, ApJ, 845, 46
Fisk, L., Schwadron, N., & Zurbuchen, T. 1998, SSRv, 86, 51
Folsom, C. P., Petit, P., Bouvier, J., et al. 2016, MNRAS, 457, 580
Gallet, F., & Bouvier, J. 2013, A&A, 556, A36
Gallet, F., & Bouvier, J. 2015, A&A, 577, A98
Garraffo, C., Cohen, O., Drake, J., & Downs, C. 2013, ApJ, 764, 32
Garraffo, C., Drake, J. J., & Cohen, O. 2015, ApJ, 813, 40
Garraffo, C., Drake, J. J., & Cohen, O. 2016a, A&A, 595, A110
Garraffo, C., Drake, J. J., & Cohen, O. 2016b, ApJL, 833, L4
Gray, D. 1984, ApJ, 277, 640
Gregory, S., Donati, J.-F., Morin, J., et al. 2012, ApJ, 755, 97
Gregory, S. G., & Donati, J.-F. 2011, AN, 332, 1027
Gregory, S. G., Donati, J.-F., & Hussain, G. A. 2016, arXiv:1609.00273
Güdel, M. 2007, LRSP, 4, 3
Hébrard, É, Donati, J.-F., Delfosse, X., et al. 2016, MNRAS, 461, 1465
Holzwarth, V. 2005, A&A, 440, 411
Hunter, J. D. 2007, CSE, 9, 90
Hussain, G. A., & Alecian, E. 2013, in IAU Symp. 302, Magnetic Fields throughout Stellar Evolution, ed. P. Petit (Cambridge: Cambridge Univ. Press), 25
Hussain, G. A., Van Ballegooijen, A., Jardine, M., & Cameron, A. C. 2002, ApJ, 575, 1078
Irwin, J., & Bouvier, J. 2009, in IAU Symp. 258, The Ages of Stars, ed. D. R. Soderblom & E. E. Mamajek (Cambridge: Cambridge Univ. Press), 363
Jeffers, S., Petit, P., Marsden, S., et al. 2014, A&A, 569, A79

Johns-Krull, C. M., & Valenti, J. A. 2000, in ASP Conf. Ser. 198, Stellar Clusters and Associations: Convection, Rotation, and Dynamos, ed. R. Pallavicini, G. Micela, & S. Sciortino (San Francisco, CA: ASP), 371
Kawaler, S. D. 1988, ApJ, 333, 236
Keppens, R., & Goedbloed, J. 1999, A&A, 343, 251
Keppens, R., & Goedbloed, J. 2000, ApJ, 530, 1036
Kochukhov, O., Petit, P., Strassmeier, K., et al. 2017, AN, 338, 428
Marcy, G. 1984, ApJ, 276, 286
Matt, S., & Pudritz, R. E. 2008, ApJ, 678, 1109
Matt, S. P., Brun, A. S., Baraffe, I., Bouvier, J., & Chabrier, G. 2015, ApJL, 799, L23
Matt, S. P., MacGregor, K. B., Pinsonneault, M. H., & Greene, T. P. 2012, ApJL, 754, L26
McFadden, P., Merrill, R., McElhinny, M., & Lee, S. 1991, JGR, 96, 3923
McQuillan, A., Aigrain, S., & Mazeh, T. 2013, MNRAS, 432, 1203
Meibom, S., Mathieu, R. D., & Stassun, K. G. 2009, ApJ, 695, 679
Meibom, S., Mathieu, R. D., Stassun, K. G., Liebesny, P., & Saar, S. H. 2011, ApJ, 733, 115
Mestel, L. 1968, MNRAS, 138, 359
Mestel, L. 1984, in Cool Stars, Stellar Systems, and the Sun, ed. S. L. Baliunas & L. Hartmann (Berlin: Springer), 49
Mignone, A. 2009, MSAIS, 13, 67
Mignone, A., Bodo, G., Massaglia, S., et al. 2007, ApJS, 170, 228
Morgenthaler, A., Petit, P., Morin, J., et al. 2011, AN, 332, 866
Morin, J., Donati, J.-F., Forveille, T., et al. 2008a, MNRAS, 384, 77
Morin, J., Donati, J.-F., Petit, P., et al. 2008b, MNRAS, 390, 567
Nicholson, B., Vidotto, A., Mengel, M., et al. 2016, MNRAS, 459, 1907
Pantolmos, G., & Matt, S. P. 2017, ApJ, 849, 83
Parker, E. 1965, SSRv, 4, 666
Petit, P., Dintrans, B., Solanki, S., et al. 2008, MNRAS, 388, 80
Pinto, R., Brun, A., & Rouillard, A. 2016, A&A, 592, A65
Pinto, R. F., Brun, A. S., Jouve, L., & Grappin, R. 2011, ApJ, 737, 72
Reiners, A. 2012, LRSP, 9, 1
Reiners, A., & Mohanty, S. 2012, ApJ, 746, 43
Réville, V., & Brun, A. S. 2017, ApJ, 850, 45
Réville, V., Brun, A. S., Matt, S. P., Strugarek, A., & Pinto, R. F. 2015, ApJ, 798, 116
Réville, V., Folsom, C. P., Strugarek, A., & Brun, A. S. 2016, ApJ, 832, 145
Riley, P., Linker, J., Mikić, Z., et al. 2006, ApJ, 653, 1510
Riley, P., & Luhmann, J. 2012, SoPh, 277, 355
Robinson, R., Worden, S., & Harvey, J. 1980, ApJL, 236, L155
Saar, S. 1990, in IAU Symp. 138, The Solar Photosphere: Structure, Convection, and Magnetic Fields, ed. J. O. Stenflo (Cambridge: Cambridge Univ. Press), 427
Saikia, S. B., Jeffers, S., Morin, J., et al. 2016, A&A, 594, A29
Schatzman, E. 1962, AnAp, 25, 18
See, V., Jardine, M., Vidotto, A., et al. 2015, MNRAS, 453, 4301
See, V., Jardine, M., Vidotto, A., et al. 2016, MNRAS, 462, 4442
See, V., Jardine, M., Vidotto, A., et al. 2017a, MNRAS, 466, 1542
See, V., Jardine, M., Vidotto, A., et al. 2017b, MNRAS, 474, 536
Skumanich, A. 1972, ApJ, 171, 565
Soderblom, D. 1983, ApJS, 53, 1
Stauffer, J., Rebull, L., Bouvier, J., et al. 2016, AJ, 152, 115
Steinolfson, R., & Hundhausen, A. 1988, JGR, 93, 14269
Testa, P., Drake, J. J., & Peres, G. 2004, ApJ, 617, 508
Ud-Doula, A., Owocki, S. P., & Townsend, R. H. 2009, MNRAS, 392, 1022
van der Holst, B., Sokolov, I. V., Meng, X., et al. 2014, ApJ, 782, 81
Van Saders, J. L., & Pinsonneault, M. H. 2013, ApJ, 776, 67
Velli, M. 2010, in AIP Conf. Proc. 1216, Twelfth International Solar Wind Conference, ed. M. Maksimovic et al. (Melville, NY: AIP), 14
Vidotto, A., Gregory, S., Jardine, M., et al. 2014, MNRAS, 441, 2361
Vidotto, A., Jardine, M., Opher, M., Donati, J., & Gombosi, T. 2011, in ASP Conf. Ser. 448, 16th Cambridge Workshop on Cool Stars, Stellar Systems, and the Sun, ed. C. M. Johns-Krull, M. K. Browning, & A. A. West (San Francisco, CA: ASP), 1293
Vidotto, A., Opher, M., Jatenco-Pereira, V., & Gombosi, T. 2009, ApJ, 699, 441
Vidotto, A., Opher, M., Jatenco-Pereira, V., & Gombosi, T. 2010, ApJ, 720, 1262
Weber, E. J., & Davis, L. 1967, ApJ, 148, 217

# Erratum "The Effect of Combined Magnetic Geometries on Thermally Driven Winds. II. Dipolar, Quadrupolar, and Octupolar Topologies" (2018, ApJ, 854, 78)

Adam J. Finley and Sean P. Matt
University of Exeter, Department of Physics & Astronomy, Stoker Road, Devon, Exeter, EX4 4QL, UK; af472@exeter.ac.uk
Received 2018 March 28; revised 2018 April 2; published 2018 April 25

In the original manuscript, Figure 5 was incorrectly printed as a copy of Figure 6. This erratum shows Figure 5 as it was intended. All tabulated data and scientific results of the paper remain unaffected.
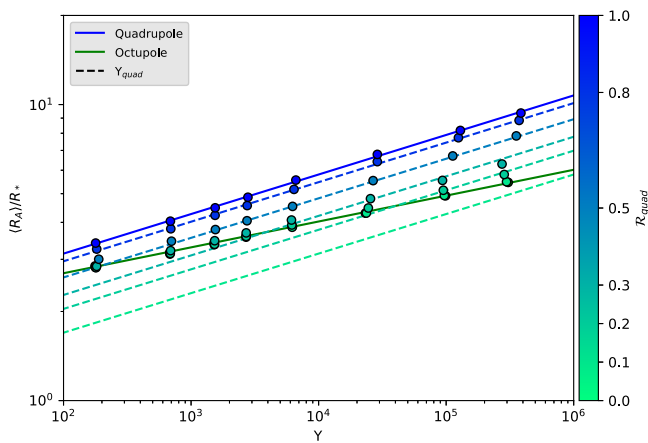


**Figure 5.** Average Alfvén radius vs. wind magnetization, $\Upsilon$, for the different combinations of quadrupole and octupole, in a similar format as Figure 3. Color-coded dashed lines relate to the prediction considering only the quadrupolar component of the field for each $\mathcal{R}_{quad}$. The combinations shown here behave in a similar manner to dipole–quadrupole combined fields, in a sense that the lower order field (with the lowest $l$) governs the Alfvén radius for large wind magnetizations, $\Upsilon$, and the higher order (large $l$) controlling the low magnetization scaling.